frontiers | Frontiers in Earth Science

ORIGINAL RESEARCH
published: 13 July 2022
doi: 10.3389/feart.2022.825679

Ocean Dynamics and Methane Plume Activity in Tatar Strait, Far Eastern Federal District, Russia as Revealed by Seawater Chemistry, Hydroacoustics, and Noble Gas Isotopes

Glen Tritch Snyder[1,2], Andrey Yatsuk[3], Naoto Takahata[1], Renat Shakirov[3], Hitoshi Tomaru[4], Kentaro Tanaka[1], Anatoly Obzhirov[3], Aleksandr Salomatin[3], Shinsuke Aoki[5], Elena Khazanova[3], Evgeniya Maryina[3], Yuji Sano[6] and Ryo Matsumoto[2]*

[1]Atmosphere and Ocean Research Institute, University of Tokyo, Kashiwa Campus, Chiba, Japan, [2]Gas Hydrate Research Laboratory, Meiji University, Ikuta Campus, Kanagawa, Japan, [3]Department Geology, V. I. Il'ichev Pacific Oceanological Institute, Vladivostok, Russia, [4]Department Earth Sciences, Chiba University, Chiba, Japan, [5]Fuel Resource Geology Group, Research Institute for Geo-Resources and Environment, National Institute of Advanced Industrial Science and Technology, Tsukuba, Japan, [6]Center for Advanced Marine Core Research, Kochi University, Kochi, Japan

OPEN ACCESS

Edited by:
Miriam Römer,
University of Bremen, Germany

Reviewed by:
Laura Lapham,
University of Maryland, United States
Tamara Baumberger,
Oregon State University, United States

***Correspondence:**
Glen Tritch Snyder
glen@aori.u-tokyo.ac.jp

Specialty section:
This article was submitted to Geochemistry, a section of the journal Frontiers in Earth Science

Received: *30 November 2021*
Accepted: *16 June 2022*
Published: *13 July 2022*

Citation:
Snyder GT, Yatsuk A, Takahata N, Shakirov R, Tomaru H, Tanaka K, Obzhirov A, Salomatin A, Aoki S, Khazanova E, Maryina E, Sano Y and Matsumoto R (2022) Ocean Dynamics and Methane Plume Activity in Tatar Strait, Far Eastern Federal District, Russia as Revealed by Seawater Chemistry, Hydroacoustics, and Noble Gas Isotopes. Front. Earth Sci. 10:825679. doi: 10.3389/feart.2022.825679

This investigation presents methane, noble gas isotopes, CTD, and stable isotopic data for water samples collected in Niskin bottles at Tatar Strait during the spring seasons of 2015 and 2019 onboard the Russian R/V Akademik M.A. Lavrentyev. The results are compared to previous research carried out in 1999 in a nearby portion of the Strait and demonstrate that salinity and temperature can change appreciably. The CTD data from 1999 shows warm surface waters underlain by cold subsurface waters. In contrast, the 2015 data show the CTD data that show warm temperatures and high salinity extending down from the surface well into intermediate waters, while the 2019 data show cold surface waters underlain by even colder subsurface waters. CTD data collected above active gas plume sites along Sakhalin Island's western shore show no substantial difference in temperature or salinity from the non-plume sites, and the methane concentrations at all of the measured sites are significantly above saturation, even in the shallow waters. Hydroacoustic data also suggest the presence of free gas and gas hydrate–coated methane bubbles from the seafloor at least to the base of upper intermediate waters. All of the intermediate and deep Japan Sea Proper waters in Tatar Strait still retain tritiogenic ^{3}He, similar to that observed throughout much of the Japan Sea, indicating limited vertical exchange between these layers and surface waters. An analysis of the δ^{13}C of dissolved inorganic carbon in the seawater shows that positive values are limited to surface waters and that the waters become progressively more depleted in ^{13}C with depth. The results are consistent with research over the past several decades which has shown that ventilation of intermediate and deep Japan Sea Proper water is somewhat limited, while both the temperature and salinity of surface and subsurface water layers within the strait are sensitive to the balance between cold,

less saline waters contributed by the Amur River/Primorye Current from the north and warm, saline waters contributed by the Tsushima Current from the south.

Keywords: methane seep, Tatar Strait, ocean circulation, helium isotopic ratios, stable carbon isotopes, hydroacoustics, salinity, Japan Sea

INTRODUCTION

Background

Recent research at Tatar Strait, located in the northernmost Japan Sea, has indicated that surface water circulation patterns may change significantly from one year to the next, influencing not only the thermal structure of the strait but also potentially influencing the distribution of zooplankton well as the abundance and migration patterns of a variety of macrofaunal species (Tarasyuk et al., 2002; Kobayashi et al., 2009; Velikanov, 2016; Dulenina et al., 2020). To provide a preliminary assessment of the potential for changes in Tatar Strait circulation, we present CTD (conductivity, temperature, and depth) results and gas chemistry obtained on research cruises during the late spring of 2015 and 2019 onboard the Russian R/V Akademik M.A. Lavrentyev (cruises LV-70 and LV-85, respectively). The data is compared to that obtained in 1999 (Postlethwaite et al., 2005) to see if measurable changes have occurred over the past two decades.

For the gas plume sites in eastern Tatar Strait, hydroacoustic data are presented showing the active release of methane from seafloor seeps at the time of sampling. We also present noble gas isotopic data and compare this with earlier noble gas isotopic determinations carried out in non-plume sites of the strait (Postlethwaite et al., 2005). There are several reasons why the noble gas isotopic analysis is a compelling procedure to elucidate ocean circulation in general, as well as the behavior of gases at both hydrothermal and cold seep sites. Mantle-derived gases are more abundant in ^{3}He, whereas radiogenic ^{4}He is generated in uranium- and thorium-rich crustal rocks such as granite. As such, ^{3}He/^{4}He ratios have been used to determine, for example, whether mantle helium is present in methane hydrates located in gas chimneys in the eastern margin of the Japan Sea (Snyder et al., 2020). Adjacent to Tatar Strait, seeps and hydrocarbon wells on Sakhalin Island have shown consistent mantle helium signatures in the southern part of the island with crustal signatures being predominant in the northern part of the island (Lavrushin et al., 1996). Some helium anomalies have been noted in seawater and sediment gas around the plume sites (Shakirov et al., 2016) yet no previous noble gas isotopic studies have determined whether this helium is derived from mantle gases relating to rifting during the opening of the Tatar Trough, or whether the helium is related to sedimentary and granitic rocks of late Cretaceous to early Eocene which were subsequently uplifted during the formation of Sakhalin Island (Glorie et al., 2017) and which by now would have accumulated measurable amounts of ^{4}He.

Anaerobic oxidation of methane (AOM) has been shown to influence the isotopic composition of dissolved inorganic carbon in the pore waters of shallow sediments associated with gas seep sites as has been the well documented in the Japan Sea. Sediment pore waters associated with AOM at gas chimney sites in Umitaka Spur, for example, yield δ^{13}C values of around −40‰ (Hiruta et al., 2015). The fate of methane in the water column is not well understood, although the implications are important given it is the potential of methane as a greenhouse gas. We look at the δ^{13}C

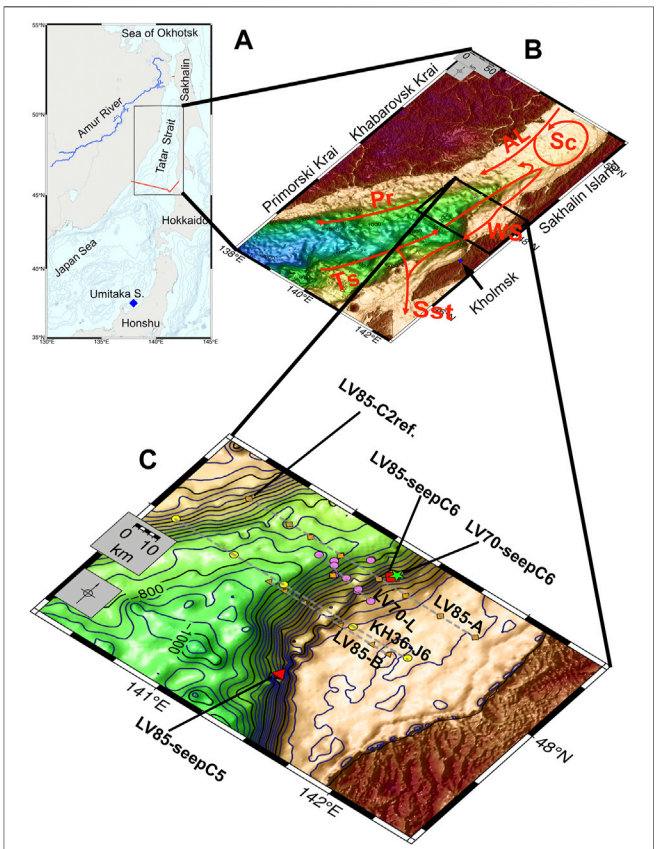

FIGURE 1 | (A) Map of Tatar Strait and the Amur River, relative to the Russian island of Sakhalin and the Japanese islands of Hokkaido and Honshu. The red line shows the current geographical boundary for Tatar Strait. The reference seep samples in this study are from Umitaka Spur in Japan Sea to the south. **(B)** Map of southern Tatar Strait with principal surface currents (After: Andreev, 2020; Pishchal'nik et al., 2010). Pr, Primorye Current; Sst, Soya Strait; WS, West Sakhalin Current; AL, Amur Liman Current; Sc, Schenk Current; Ts, Tsushima Current. Shelf areas (<500 m) of the strait are shaded in light brown. Deeper areas of the strait comprising Tatar Trough (>500 m) are shaded in green and blue. **(C)** Study area is located between 47°30′N and 48°30′N, near the Trough transitions from intermediate to shallow depths. Orange represents transects LV85 A&B sampled in 5/2019 and Violet represents LV70-L transect sampled in 6/2015. Yellow represents sites from KH36 sampled in 7/1999 and reported previously (Postlethwaite et al., 2005). Red represents Plume seep-C5 and seep-C6 from LV85. Green star represents Plume seep-C6 from LV70.

values of dissolved inorganic carbon (DIC) in one plume site in Tatar Strait, to see if methane oxidation in the water column is significantly large to influence the dissolved carbon pool within the water column. In addition, we calculate methane oversaturation in the shallow waters at the sampled plume sites and compare it with a reference site to see if it is significantly higher.

Study Area

Tatar Strait is situated at the northernmost part of the Japan Sea, between Sakhalin Island and the Russian Far Eastern districts of Primorski Krai and Khabarovsk Krai (**Figure 1A**). The northernmost extent of Tatar Strait comprises the 7.2 m deep Amur Estuary at 53.7°N which is located to the south of the Amur River mouth. The southern geographical boundary of Tatar Strait begins at the tip of Sakhalin Island at 45.9°N, extends just south of the Japanese Islands of Rebun and Rishiri, and then continues back up to 45.9°N in Primorski Krai (red line on **Figure 1A**) (Danchenkov, 2004). This boundary is for the most part geopolitical, in that there are no bathymetric features which either distinguish or isolate the southern extent of Tatar Strait from the rest of the Japan Sea. Water depths in the central southern portion of the strait are just over 2000 m, forming the Tatar Trough (blue- and green-shaded areas in **Figure 1B**), whereas north of 48.5° the Tatar Strait narrows and the waters are all shallower than 500 m (tan-shaded areas in **Figure 1B**).

Water circulation into the strait is limited to the Tsushima Current, which flows northward along the length of the Japan Sea, and to the Amur Liman Current, which flows from the mouth of the Amur River into the northern reaches of Tatar Strait (**Figure 1B**). The outflow of waters from the strait is either back into the Japan Sea along the western margin by means of the Primorye Current, or through Soya Strait and into the Okhotsk Sea, between the islands of Sakhalin and Hokkaido by means of the West Sakhalin Current. Internal circulation within the strait is quite variable but includes the West Sakhalin and the Schrenk currents (Andreev, 2018; Pishchal'nik et al., 2010). As will be discussed, the vertical structure of water masses in Tatar Strait can also be influenced by the variable influx of waters from either the Amur Liman Current, or from the Tsushima Current. This influence can extend through the shallow surface and subsurface waters, all the way down to the upper intermediate waters (Danchenkov, 2004).

Our study area is located between 47.5°N and 48.5°N in Tatar Strait (**Figure 1C**), including the eastern margin of the strait where abundant gas seep plumes are located, deeper central portion of the trough, and seep-free portion of the trough on the eastern margin (Shakirov et al., 2019; Yatsuk et al., 2020). The water depth is sufficient in the study areas to preserve the vertical water mass structure (Danchenkov, 2004), and the study area also includes the northern portion of the deep Tatar Trough. There are four sampling transects (**Figure 1C**) running roughly parallel from north to south: LV85-A sampled from 5/21 to 5/22, 2019; LV70-L sampled from 6/21 to 6/24, 2015; KH36-J6 sampled from 7/28 to 7/29, 1999; and LV85-B sampled in 5/23, 2019. A number of areas off the transects but above active gas plumes from the eastern margin of the strait were sampled around the same time as the transects, including LV85-seepsC5, LV85-seepC6, and LV70-seepC6. To provide a non-seep reference for comparison, site LV85-C2ref., located on the farthest west on the northernmost transect was selected for more detailed study.

SAMPLING AND ANALYSES

Hydroacoustic observations were carried out during both the June 2015 (LV70) and May 2019 (LV85) cruises using the sonar system of the R/V Akademik M.A. Lavrentyev, which consists of echo sounders Sargan-EM and ELAC, sonar Sargan-GM, a multichannel digital registration system, and a GPS system. The hydroacoustic system provides simultaneous registration of echo signals up to four independent channels with frequencies of 12, 20, and 135 kHz (Salomatin et al., 2014). At a time of acoustic measurements, accurate vessel's coordinates were determined with GPS and using the operating frequencies of 20 kHz with a beam width of 10°.

During both the LV70 and LV85 cruises, a Sea-Bird SBE-9 CTD and Niskin Rosette system were deployed. Water column salinity, temperature, and depth data were recorded over 1 s intervals and processed using Seasave ver. 7.26.2.13 (**Supplementary Data**). Seawater turbidity was also determined using a SeaPoint Turbidity Meter which operates with an 880 nm light source at scattering angles between 15° and 150°, with peak sensitivity covering approximately 90°. Turbidity measurements are reported in Formazin Turbidity Units (FTU). Upon shipboard recovery, water from the Niskin bottles was immediately transferred into 68 ml glass sample bottles which were hermetically sealed. The samples were then analyzed onboard the R/V Akademik M.A. Lavrentyev for dissolved gases (methane, hydrocarbon gases, carbon dioxide, nitrogen, and oxygen) using shipboard gas chromatographic instrumentation as described in Vereshchagina et al. (2013) and Shakirov et al. (2019). In order to create headspace gas in the 68 ml bottles, 12 ml high-purity helium was injected through the rubber septum. After this, samples were shaken on a LS-110 mixing device to reach equilibrium between the liquid and the gas phases. After mixing, an aliquot of the gas phase (4 ml) was taken up by a syringe for a gas chromatographic analysis. Onboard gas analysis was performed with a "KRISTALLUX-4000M" gas chromatograph ("Meta-Chrom", Yoshkar-Ola, Russia). The chromatograph has three detectors: two thermal conductivity (TCD) and one flame ionization (FID) detectors. FID allows one to study the quantitative content of hydrocarbon composition (C_1–C_6) with a sensitivity of 10^{-6}%. Inorganic gases such as nitrogen, oxygen, and carbon dioxide, as well as methane with a concentration of more than 1%, are analyzed on a TCD, the sensitivity of which is 0.01%. The gas chromatograph had two packed columns: HayeSep R column, 2.5 m length, 2.5 mm i.d., 80/100, "Meta-Chrome"; NaA column, 3 m length, 3 mm i.d., 60/80. The temperature program of the chromatographic column was isothermal—50 °C, 5 min hold. Temperature detectors were set at 195 °C for the evaporator and 160 °C for the carrier gas

which was ultrapure helium. The carrier gas flow rate was set at 20 ml/min for helium, 30 ml/min for hydrogen, and 250 ml/min for air. Calibration gas mixtures of methane were manufactured by PGS Service (1, 10, 20, 100, and 1000 ppm and 1%). The relative error of measurements did not exceed 5%. The laboratory gas geochemistry, POI FEB RAS is certified for measurements by Rosstandart (Federal Agency on Technical Regulating and Metrology, Russia). The concentrations of methane dissolved in seawater were calculated by technique described by Yamamoto et al. (1976) and modified by Wiesenburg and Guinasso (1979), using the solubility constants of the gases and are reported in nmol/L (**Table 2**). Oxygen concentrations were used to determine if the samples were subject to air contamination, and in one case (**Table 2**, LV85-5–150 m) the sample results were discarded and not considered in the figures or data analysis.

In addition to the aforementioned sampling and analyses, two additional sample splits were collected during LV85 from seepC6 and seepC5 (**Figure 1C**). Seawater samples were transferred directly from the Niskin bottles to copper tubing for later noble gas analysis using the procedures described in Takahata et al. (2008). In addition, for seepC5, 100 ml of seawater aliquots were filtered and introduced into evacuated flasks which each contained 100 mg sulfamic acid using a method adapted from Atekwana and Krishnamurthy (1998) and also employed at submarine seep sites by Hiruta et al. (2015) for later determination of the $\delta^{13}C$ values for dissolved inorganic carbon (DIC). Solid, reagent-grade sulfamic acid (HOS_2NH_2) was used, rather than phosphoric acid employed in the method of Atekwana and Krisnamurthy (1998), due to its ease in handling under shipboard conditions (Kawagucci et al., 2013). In addition, during cruise LV-85, the atmospheric methane concentrations were determined using a Picarro gas concentration analyzer so that the flux of methane from shallow water to the atmosphere could later be calculated above the two sites LV85-seepC6 and LV85-seepC5 as well as above a reference site (LV85-C2ref.) shown in **Figure 1C**.

At the end of the cruise, both the sealed copper tubes and the glass flasks for the DIC analysis were shipped from Vladivostok to the Atmosphere and Ocean Research Institute (AORI), University of Tokyo, Japan for analysis at the Noble Gas Isotope Laboratory. For noble gas isotopic composition, the dissolved gas in the seawater was transferred from the copper tubing using methods described in Takahata et al. (2008). The procedures for the noble gas isotopic analysis are described in Sano and Nakjima, (2008) and Park et al.(2006). Helium and neon were separated from the gas using a combination of charcoal traps kept at liquid nitrogen temperature as well as hot titanium getters. The ratios of $^{20}Ne/^{4}He$ were determined using a Pfeiffer Vacuum Prisma quadrupole mass spectrometer. Helium was separated from neon using a 40K charcoal trap. Helium isotopic composition was determined using a GV Instruments Helix SFT noble gas mass spectrometer, and the ratios of $^{3}He/^{4}He$ were normalized to the air ratio (R_A=1.4 x 10^{-6}). Precision of the $^{3}He/^{4}He$ ratios is ± 0.01 R_A. The results are listed in **Table 2**. Of the 18 samples analyzed from the gas plumes, two samples showed signs of atmospheric contamination with $^{20}Ne/^{4}He$ similar to the air ratio of 3.14. The noble gas isotopic composition was not further considered for the two air-contaminated samples which were LV85-seepC5–12 (0 m water depth) and LV85-seepC6–2 (316 m water depth) due to air contamination.

For the stable isotopic composition of DIC, the gas sample in the headspace of the sampling bottle (5–10 ml), including CO_2 liberated from DIC, was transferred to a glass vial, which was pre-filled with pure helium. The carbon isotope ratio of samples was then measured with a conventional continuous flow mass spectrometer (Delta V plus, Thermo Fisher Scientific). The carbon isotope ratio is expressed as conventional delta notation ($\delta^{13}C$) with respect to Pee Dee Belemnite (PDB). NBS-19 ($\delta^{13}C$=1.95‰) served as the standard material to determine $\delta^{13}C$ of the sample. Repeated analyses of NBS-19 yielded the reproducibility of $\delta^{13}C$ measurement better than ± 0.2‰. After measuring the reference CO_2 gas three times, the sample CO_2 gas was analyzed six times. The standard deviation for sample gas varied from 0.02‰ to 0.1‰, depending on the intensity.

RESULTS

In order to provide a consistent depth reference, the results are presented in the context of the eight recognizable water masses, as described by Danchenkov (2004), which provide the vertical seawater structure found in Tatar Strait (**Figure 2**) and are consistent with water layers found in the Japan Sea in general. The water masses have been numbered in the figures and discussion as follows: a surface water mass (I) which generally extends down to around 40 m. In areas where the Tsushima Current is present, surface water (I) may be subtropical and saline (>34.1 Practical Saline Units, PSU). In other areas where the surface water is influenced more by the Amur and Primorye currents, surface water (I) is subarctic, cold, and has low salinity. A subsurface water mass (II) is generally restricted to the upper 75 m and may consist of either subtropical or subarctic water and depending on which is denser than the prevailing surface waters. Below the surface (I) and subsurface (II) waters are intermediate waters (III). Just as the Japan Sea in general may be characterized by intermediate and central waters (Jenkins, 2008), Tatar Strait intermediate waters are subdivided into upper (IIIa) and lower (IIIb) water masses. The upper (IIIa) is slightly warmer with low-salinity (33.96–34.04 PSU, 3–4 °C), while the lower (IIIb) is colder and with high-salinity (>34.06 PSU, 1–2 °C). The relative thickness of IIIa and IIIb is variable, but the combined intermediate water mass extends from 75 to 300 m. Below 300 m is the deep Japan Sea Proper water mass (IV) with temperatures indistinguishable from those of the rest of the Japan Sea deep waters at 0.12–1.2 °C and salinities of 34.05–34.08 PSU. Finally, a slightly warmer bottom water mass (V) can be present just above the seafloor, but it is found only in the deepest parts of the Tatar Trough located to the south of our study area and need not be considered in this study.

Hydroacoustic Flares at Methane Seep Sites

Methane seeps from the eastern margin of Tatar Strait are readily identified by hydroacoustic flares, or areas of high reflection intensity in the echograms which are shown plotted against time (**Figure 3**), and are situated at depths of 300–350 m. The hydroacoustic flare at the site LV85-seepC6 was observed in 2019 (**Figure 3A**) and is from the same gas chimney structure as the site LV70-seepC6 in 2015 (**Figure 3B**), while the site LV85-seepC5 is situated along the same margin, but to the south (**Figure 3C**). The reference site LV85-C2ref. is situated 64 km to the west of plume LV85-seepC6, (**Figure 1C**) along transect LV85-A and does not show any evidence of flaring at all (**Figure 3D**). Where flares are apparent, the highest reflection intensity is in deep Japan Sea Proper water (IV) and attenuates as the gas rises through lower intermediate water (IIIb), disappearing completely toward the top of upper intermediate water (IIIa) and subsurface water (II).

In addition, all of the echograms in this study reveal a number of reflective areas or sound scattering layers (SSL), including the reference site, (**Figure 3D**) which do not appear to be related to gas seep activity or rising gas bubbles. The SSL are most intense in the Surface (I) and Subsurface (II), although similar layering is observed in lower intermediate (IIIb) water.

Salinity and Temperature Trends Along the Transects Crossing the Strait

Depth profiles were constructed with salinity (in Practical Salinity Units, PSU) and temperature (^{o}C) as well as turbidity (in Nephelometric Turbidity Units, NTU). The data from the 2015 and 2019 cruises in this study (**Supplementary Data**), as well as those of those of the 1999 cruise, (Postlethwaite et al., 2005) are plotted against depth (**Figures 4A,B**). Turbidity was not available from the 1999 study, so the depth profile for turbidity only considers data from 2015 to 2019.

As can be observed with the temperature depth profiles (**Figure 4A**), samples show a strong temperature minimum at the boundary between surface (I) and sub-surface (II) waters in 1999 (KH36) and 2019 (LV85). This boundary appears to be missing in 2015 (LV70). In addition, with the 2015 sites, there is an inflection at or just above the boundary between upper (IIIa) and lower (IIIb) water masses. Both 1999 (KH36) and 2015 (LV70) waters show higher temperatures in the surface and subsurface waters than that observed in 2019 (LV85). These differences decrease with depth, but do extend all the way to the base of the lower intermediate waters (IIIb). For each of the given years, there are no apparent differences between the different cross-basin transects, nor is there an apparent difference between seep temperatures and the temperatures of non-seep transect sites.

Salinity increases rapidly with depth in the surface waters (**Figure 4B**). For both 1999 (KH36) and 2015 (LV70), the salinities largely coincide as opposed to the less saline 2019 (LV85) samples. For both KH36 and LV70, salinities reach maximum values in the shallow subsurface (II), as opposed to the LV85 sites where salinity continues to increase until the base of the upper intermediate (IIIa) waters. Turbidity is, in all cases, greatest in the deepest waters of all sites, regardless of what depth that actually is (**Figure 4C**). The 2015 LV70 transect-C sites show an increase in turbidity with depth in surface waters (I), followed by a decrease in the sub-surface (II), followed by fairly constant turbidity until the waters near the bottom. This increase coincides with the area of SSL in the hydroacoustic data associated with the nearby plume (**Figure 3C**), which will be further discussed.

A cross-plot of salinity versus temperature (**Figure 4D**) clearly shows how the water compositions converge in the deeper Japan Sea Proper waters (IV), but diverge greatly in the shallow subsurface (II) and surface waters (I). In addition to the CTD data, isopycnal lines were calculated using the UNESCO formula (Massel, 2015) and plotted in the same figure. The most recent waters from 5/2019 (LV85) trend toward low-salinity, low-temperature sub-arctic waters. The next most recent waters from 6/2015 (LV70) show the greatest influence of shallow, high-salinity subtropical waters. Waters from two decades previous, in 7/1999 (KH36), are situated in-between those of the two most recent cruises. It is interesting that shallow and intermediate waters can vary greatly from year to year, but the overall density trend with depth remains constant with low-salinity and cold shallow and intermediate water masses having nearly the same density as high-salinity warm waters from the same water masses.

In order to visually evaluate the spatial distribution of temperature and salinity in the water column, Generic Mapping Tools (Wessel et al., 2019) was used to interpolate between the CTD sites for transects in 2019, 2015, and 1999 (**Figures 5**, **6**; **Supplementary Figures S1, S2**). The seafloor position was mapped according to Gebco's Bathymetry Data (IOC, IHO and BODC, 2003). The transects studied include the northernmost deep portion of the trough (**Figure 1C**).

Cross-basin temperature profiles (**Figure 5**) clearly show layering consistent with that of the depth profile in **Figure 4A**. Both 2019 (LV85) sections (**Figures 5A,B**) show a warm surface water mass underlain by cold sub-surface waters and slightly warmer intermediate waters underlain by colder deep waters. The 1999 section (**Figure 5C**) shows surprisingly little difference when compared to the corresponding nearby 2019 section (**Figure 5B**), despite two decades having elapsed between the two cruises. The surface waters are warmer for 1999 (as seen in **Figure 4B**), perhaps since they were sampled in July rather than in May, but temperatures in the sub-surface waters and deeper are not discernible from 2019. Very striking differences are observed in 2015, however, where there are high temperatures which extend from the surface through the subsurface, and even somewhat into the intermediate waters (**Figures 4A**, **5D**). Data from the 2019 transects were combined with the data from the two plume sites of that year to see anomalies in surface and bottom waters (**Supplementary Figure S1**). In general, a plume of somewhat cooler waters (by about 2 $^{\circ}$C) seems to extend over the surface waters from north to south, just west of the slope on the Sakhalin Island side of the trough. Bottom waters are uniformly cold at near-

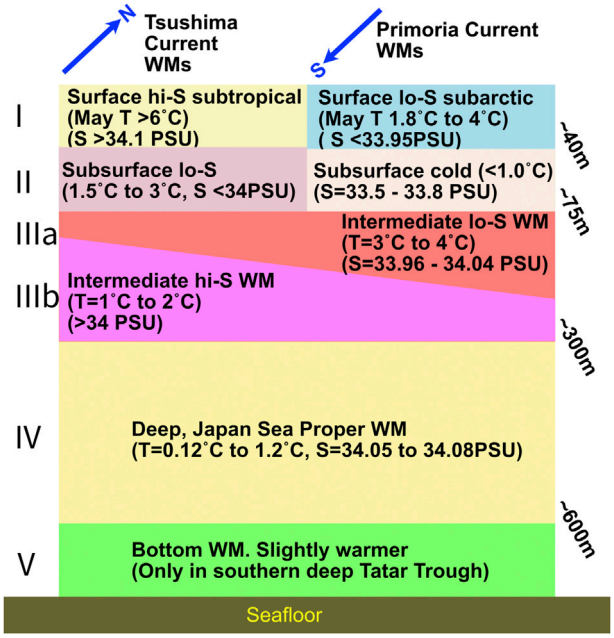

FIGURE 2 | Vertical structure of in Tatar Strait seawater showing eight discernible water masses (after Danchenkov, 2004). Surface (I), subsurface (II), and intermediate (IIIa, b) water masses are influenced by changes in the relative amounts of water from the southbound Primorye Current and the northward migrating Tsushima Current. Japan Sea Proper water (IV) is generally found below 300 m and shows less variation. Slightly warmer bottom waters (V) are found only in the part of Tatar Trough to the south of our study area.

zero temperatures throughout the sampled area, with only slightly warm bottom waters in the shallowest site which is closest to the Sakhalin coast.

Cross-basin profiles of salinity also demonstrate how different the 2015 data is. Both of the 2019 profiles (**Figures 6A,B**) show very dilute surface waters, underlain by somewhat more saline subsurface waters, and intermediate waters that are slightly less saline than the deep waters. Once again, the 1999 waters from Postlethwaite et al. (2005) are not appreciably different (**Figure 5C**) from those of 2019. In contrast, the 2015 profile (**Figure 5D**) shows saline surface waters, very saline subsurface waters, slightly less saline intermediate waters, and finally saline deep waters. The most striking feature in the 2015 profile is the highly saline subsurface waters, clearly influenced by the subtropical Tsushima Current. As with temperature, the interpolated salinity values from 2019 were also mapped for surface and bottom waters (**Supplementary Figure S2**). On the surface, areas of slightly greater salinity are observed both to the west and to the east of the low-temperature surface waters (shown in **Supplementary Figure S1A**); however, a clearly-lineated low-salinity plume is not observed. Bottom waters are uniformly more saline (**Supplementary Figure S2B**), with the exception of slightly less saline waters on the margins of Sakhalin Island. Still, in 2019, surface waters are less saline than bottom waters, even along the coastal margin.

Plume Site Depth Trends and Methane Concentrations

One point of interest with submarine gas seeps is the depth of hydrate stability within the water column in the area where the gas is ascending. The phase boundary between pure methane hydrate and methane gas in seawater was calculated using the following simplified relationship (Dickens and Quinby-Hunt, 1994):

$$T^{-1} = 3.79 \times 10^{-3} - 2.83 \times 10^{-4} (logP), \quad [1]$$

where T is temperature in K, P is pressure in MPa, and the pressure gradient is assumed to be 1 x 10^{-2} MPa/m.

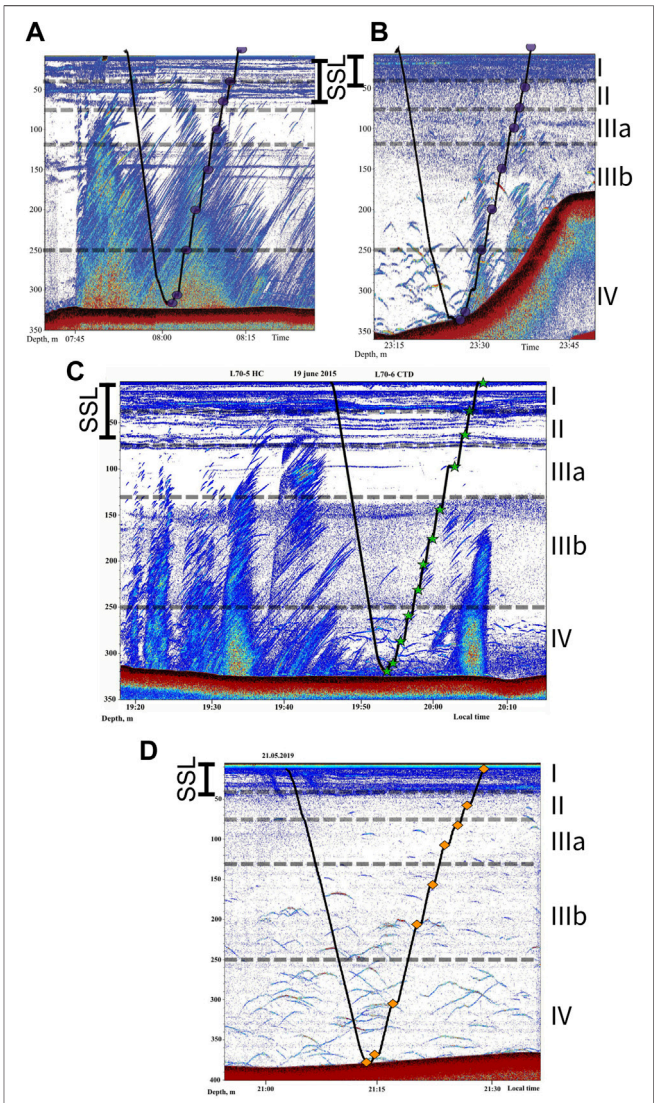

FIGURE 3 | (A) Hydroacoustic data, depth versus time, for LV85-seepC6, showing the gas plume position as well as the position of the CTD during sampling during 5/2019. Sound scattering layers (SSL) infer the presence of zooplankton in the upper 50–70 m and possibly deeper. **(B)** Hydroacoustic data for LV85-seepC5 sampled during 5/2019. **(C)** Hydroacoustic data for LV70-seepC6, sampled during 6/2015 adjacent to the same location as LV85-seepC6. **(D)** Hydroacoustic data for reference site LV85-C2ref., located on the western margin where there are no gas plumes.

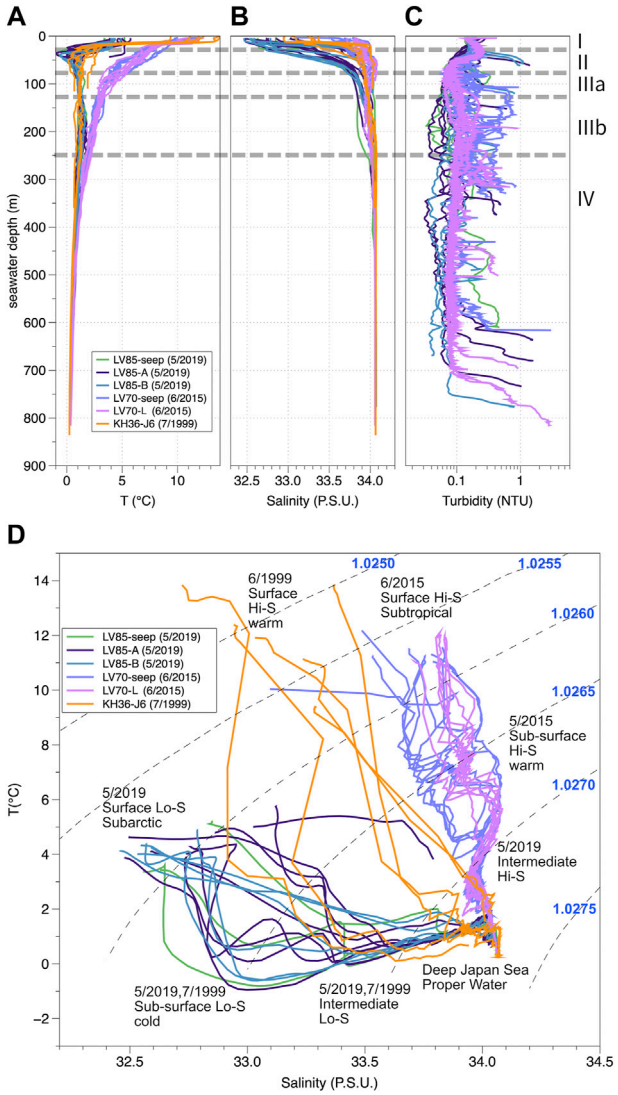

FIGURE 4 | Water column salinity and temperature profiles determined from CTD data. Isopycnal lines (g/cm^3) calculated from the UNESCO formula (Massel, 2015). Appreciable changes have occurred from between the three sampling years in shallow to upper intermediate waters. **(A)** Temperature profiles show warm surface waters (I) in 1999 and 2015. Cold subsurface waters (II) are observed in both 1999 and 2019. Temperatures from each sampling year converge in the Deep Japan Sea Proper water mass (IV). In both 2015 and 2019, there is no appreciable difference in the temperatures was observed for seep and non-seep sites. **(B)** Salinity profiles show the highest values in lower surface (I) and subsurface waters (II) collected in 2015 and 1999. As with temperature, there is that are largely coincident in lower intermediate (IIIb) and Japan Sea proper (IV) waters. **(C)** Turbidity is generally greatest in samples closest to the seafloor; however, some inflections occur between water layers. **(D)** Temperature-salinity plot showing that while samples from 1999, 2015, and 2019 diverge in surface (I) and sub-surface water masses (II), they still fall into similar density fields for any give depth. The samples from all three years converge with depth in the Japan Sea Proper water mass (IV).

The CTD data is matched with intervals where the Niskin bottle water was sampled (**Table 1**), in order to provide a direct comparison with gas chemistry and isotopic composition (**Table 2**). In order to compare seawater above the plume sites (LV70-seepC6, LV85-seepC6, and LV85-seepC5), the reference site located at a similar depth on the western margin of Tatar Strait is also included (LV85-C2ref., **Figure 1C**), as well as the non-plume sites with noble gas data sampled in 1999 (Postlethwaite et al., 2005). Also presented for comparison are data from a major plume site Umitaka Spur (Saegusa et al., 2007; Takahata et al., 2008), which is located in the Japan Sea just offshore Niigata Prefecture and 1200 km to the southeast of our study area (**Figure 1A**), collected in 5/2005. As can be observed (**Figure 7A**), the temperatures for all of the sites converge near the top of the Japan Sea Proper water mass (IV), between 250 and 300 m. It is also apparent that waters in the deep Japan Sea Proper waters (IV) can host stable gas hydrate, including at the base of plume sites LV70-seepC6, LV85-seepC5, and LV85-seepC6 as well as through much of the water column in the central portion of Tatar Trough and in Umitaka Spur. At depths of ~900 m, as observed in Umitaka Spur, hydrate can be stable in seawater at temperatures below 10 °C. This is much warmer than the deep Japan Sea Proper (IV) waters at ~0.4 °C, which could host rising gas hydrate bubbles to depths shallow as 313 m.

Both temperature (**Figure 7A**) and salinity (**Figure 7B**) were combined with pressure to calculate water density in g/cm^3 (**Figure 7C**) using the UNESCO formula (Massel, 2015). Unlike temperature and salinity which can vary significantly in surface (I) and subsurface (II) between sampling years and localities, density largely coincides between the different sampling years and localities. From surface (I) to subsurface (II) there is a rapid increase in density followed by a gradual, nearly linear increase in density from subsurface (II) to deep Japan Sea Proper waters (IV).

Methane concentrations for the plume and reference sites are shown plotted against depth (**Figure 7D**). Many of the LV85 plume samples are not appreciably different from the reference site (LV85-C2Ref.), with the exception of some elevated values near the top of the deep Japan Sea Proper waters (IV) and a few high values in the upper intermediate (IIIa) and lower intermediate (IIIb) waters. Water sampled in 2015 at the site LV70-C6, however, shows uniformly higher values than the LV85 plumes and reference site, with one extremely high methane concentration in the subsurface (II).

As has been documented previously (Shakirov et al., 2019), methane concentrations can exceed saturation around the Tatar Strait plume sites. To determine to what degree oversaturation is present, the oversaturation ratio (SR) for methane (Kudo et al., 2018) was determined as follows:

$$SR(\%) = ([[CH4]_w/[CH4]_a] - 1) \times 100\%, \quad [2]$$

where $[CH4]_w$ and $[CH_4]_a$ are the observed concentration in seawater and the calculated saturation concentration of dissolved atmospheric methane in seawater, respectively. The value of $[CH_4]_a$ in nmol/L is calculated as follows:

$$ln[CH_4]_a = ln f_G + A_1 + A_2(100/T) + A_3 ln(T/100) + A_4(T/100) + S[B + B(T/100) + B(T/100)^2], \quad [3]$$

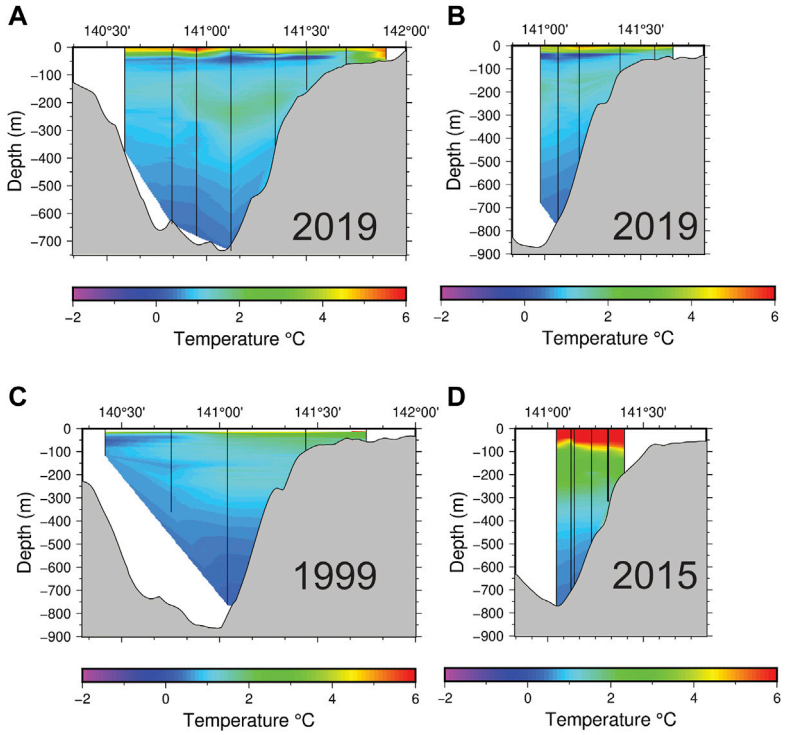

FIGURE 5 | (A) Cross-basin temperature transect in 5/2019, showing shallow warm surface waters underlain by cold subsurface, slightly warmer intermediate and cold deep waters. **(B)** Shorter transect to the south, showing similar thermal layering. **(C)** Similar cross-basin transect from 7/1999, shows cooler waters in the shallow western portion of the basin, along the Primorye coast and warmer along the Sakhalin coast. **(D)** Extremely warm shallow and intermediate waters in 6/2015.

where f_G is the concentration of atmospheric CH_4 in ppmv, T is seawater temperature in K, S is salinity in PSU, and the coefficients for solubility concentration in nmol/L are (Wiesenburg and Guinasso, 1979) A_1 = −415.2807, A_2 = 596.8104, A_3 = 379.2599, A_4 = −62.0764, B_1 = −0.05916, B_2 = 0.032174, and B_3 = −0.0048198. The atmospheric f_G is generally around 2 ppmv. Actual atmospheric values were measured onboard the R/V Akademik M.A. Lavrentyev during cruise LV85 at the time of Niskin bottle sampling (**Supplementary Table S3**) and range from 1.89 ppmv to 2.02 ppmv. For LV70-seepC6, we assume the same atmospheric concentration for LV85-seepC6 of 1.97 ppmv. For Umitaka Spur, we assume an atmospheric f_G = 1.89 ppmv (Kudo et al., 2018). Both methane concentrations in nmol/L and the derived SR are reported in **Supplementary Table S1**. Methane gas concentrations were not measured for the 1999 KH-76 cruise (Postlethwaite et al., 2005).

It is worth noting that this approach, as applied to this study and others (e.g., Kudo et al., 2018) does not contain a pressure term and only calculates the percent saturation relative to surface conditions. Nonetheless, it does provide a means of comparison over time and between sites which integrates measured headspace gas, seawater temperature, and salinity. Using this approach, the waters above the gas plumes as well as the reference sites show positive oversaturation ratios throughout the range of measurement depths (**Figure 7E**), meaning gas would exsolve from such water when brought to the surface. In some cases, a shallow maximum oversaturation occurs at 50–75 m depth, either in the subsurface (II) or the top of the upper intermediate (IIIa) waters. For the 2019 reference site LV85-C2ref., the maximum is 205% at 50 m. For the 2015 plume gas sample LV70-seepC6, the corresponding shallow maximum oversaturation value is 5212% at 60 m. Other sites have deeper maximum saturation ratios, either near the seafloor or at the boundary between upper and lower intermediate (IIIb) waters, or between lower intermediate (IIIb) waters and Japan Sea Proper (IV) waters. For example, at 305 m depth LV85-seepC6 reaches a methane oversaturation ratio of 2386%, while at 200 m LV85-seepC5 reaches an oversaturation ratio of 3740% (**Table 2**).

Noble Gas Isotopic Composition in Seawater Above plumes and Reference Sites

The noble gas isotopic composition was determined for two plume sites in Tatar Strait from cruise LV85 (**Table 2**), which we compared with the previously mentioned Umitaka Spur plume site (Saegusa et al., 2007; Takahata et al., 2008). Because the availability of noble gas sampling materials was somewhat limited on cruise LV85, we did not sample the reference site but instead compared our results with the 1999 noble gas determinations from non-plume sites (Postlethwaite et al., 2005).

Seawater in the Japan Sea generally does not show measurable amounts of mantle helium (Postlethwaite et al., 2005; Takahata

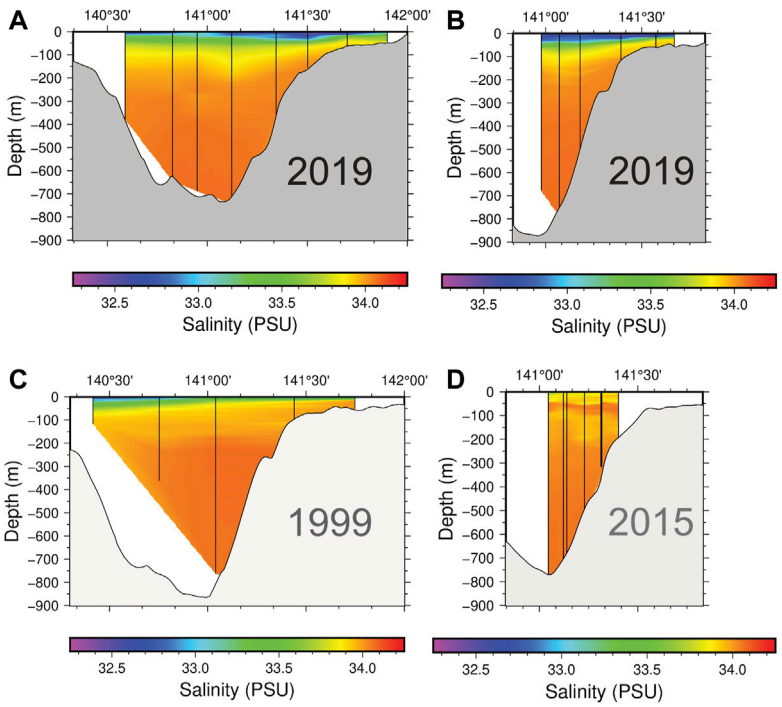

FIGURE 6 | Salinity values in southern Tatar Trough. **(A)** Cross-basin profile in 5/2019 show less saline surface, sub-surface, and upper intermediate waters. **(B)** Transect to the south from 5/2019 shows similar layering. **(C)** Profile from 7/1999 shows the less saline surface water mass and subsurface low salinity water mass are thicker on the Primorye side of the basin than the Sakhalin Side. **(D)** Short transect from 6/2015 shows predominantly high salinity waters, particularly in the subsurface.

et al., 2008) and the samples in this study are no exception. Since the changes in $^3He/^4He$ ratios are small, it is convenient to refer to the helium isotopic composition using delta notation.

$$\delta^3He = \frac{\left[\frac{^3He}{^4He}\right]_{samp.} - \left[\frac{^3He}{^4He}\right]_{air}}{\left[\frac{^3He}{^4He}\right]_{air}} X\ 100\%, \qquad [4]$$

where $R_{air} = {}^3He/{}^4He_{air} = 1.4 \times 10^{-6}$.

We report both air-normalized $^3He/^4He$ ratios and δ^3He values for the plumes and reference sites. Depth profiles (**Figure 7F**) show a near-linear increase in δ^3He which is observed for both the Umitaka Spur and Tatar Strait samples, starting at air-saturated seawater values ($\delta^3He = -1.5\%$) in surface (I) waters to 5%–7% in the upper portions of Japan Sea Proper (IV) waters. The δ^3He values for Tatar Strait waters increase more rapidly with depth than the Umitaka Spur values, reaching maximum values at 200–300 m above the seafloor. These increases are fairly typical of Japan Sea and elsewhere and are not due to the admixture of relatively ^3He-enriched mantle gas from the seafloor, but rather contributions of tritiogenic ^3He produced during the surface nuclear weapons testing in the mid-1960's. The presence of tritiogenic ^3He provides some indication of the limited exchange of water masses between shallow surface (I) and subsurface (II) waters, with the older, deeper intermediate (III) and Japan Sea Proper (IV) water masses (Postlethwaite et al., 2005; Jenkins, 2008; Takahata et al., 2008; Gamo et al., 2014). Tritium undergoes β-decay producing both a β electron (e−) and an antineutrino ($\bar{\nu}$):

$$^3H \rightarrow {}^3He + e^- + \bar{\nu}, \qquad t_{\frac{1}{2}} = 12.43yr. \qquad [5]$$

Given the short half-life, practically all of the anthropogenic tritium from the 1960's has decayed to ^3He. Although tritium analyses were not measured in this study, previous studies have shown the correlation between ^3H and δ^3He values in intermediate and deep waters which are similar to those found in this study (Postlethwaite et al., 2005; Takahata et al., 2008).

The ratios of $^{20}Ne/^4H$ also give some indication of the amount of helium added to air-saturated seawater from sources such as mantle gases and radiogenic sources. As will be shown, however, the ratios are also temperature dependent and at lower temperatures, the solubility of helium increases more relative to neon. Salinity also has an influence, although in the conditions of this study, much less than temperature. A useful method for discussing the relative amount of neon and helium is a deviation from the equilibrium solubility ratio under the observed temperature and solubility conditions (after Nicholson et al., 2011).

$$\Delta\frac{^{20}Ne}{^4He} = \frac{\left[\frac{^{20}Ne}{^4He}\right]_{samp.} - \left[\frac{^{20}Ne}{^4He}\right]_{eq.}}{\left[\frac{^{20}Ne}{^4He}\right]_{eq.}} X\ 100\%. \qquad [6]$$

The equilibrium solubility ratios $\left[\frac{^{20}Ne}{^4He}\right]_{eq.}$ were calculated using the Bunsen solubilities for each gas using experimentally

TABLE 1 | Location and depth of samples collected with Niskin bottles, as well as corresponding temperature and salinity from CTD. Density is calculated from pressure, temperature, and salinity (Massel, 2015).

Cruise	Site	Date	Long.	Lat.	Depth	Temperature	Salinity	Density (ρ)
			(E)	(N)	(m)	(˚C)	(PSU)	(g/cm^3)
Tatar Strait Slope Seeps [1]								
LV-85	C5	05/23/2019	141.367	47.722	0	4.331	32.593	1.025990
LV-85	C5	05/23/2019	141.367	47.722	50	1.064	33.875	1.027290
LV-85	C5	05/23/2019	141.367	47.722	75	1.165	33.933	1.027330
LV-85	C5	05/23/2019	141.367	47.722	100	1.582	34.035	1.027383
LV-85	C5	05/23/2019	141.367	47.722	150	1.356	34.051	1.027412
LV-85	C5	05/23/2019	141.367	47.722	200	0.969	34.057	1.027432
LV-85	C5	05/23/2019	141.367	47.722	250	0.969	34.057	1.027442
LV-85	C5	05/23/2019	141.367	47.722	326	0.885	34.058	1.027448
LV-85	C5	05/23/2019	141.367	47.722	336	0.885	34.058	1.027448
LV-85	C6	05/23/2019	141.392	47.982	0.15	3.382	32.556	1.026053
LV-85	C6	05/23/2019	141.392	47.982	40	−0.708	33.128	1.026781
LV-85	C6	05/23/2019	141.392	47.982	75	0.303	33.585	1.027103
LV-85	C6	05/23/2019	141.392	47.982	100	1.079	33.868	1.027284
LV-85	C6	05/23/2019	141.392	47.982	150	1.622	33.993	1.027346
LV-85	C6	05/23/2019	141.392	47.982	200	1.658	34.035	1.027377
LV-85	C6	05/23/2019	141.392	47.982	250	1.233	34.033	1.027405
LV-85	C6	05/23/2019	141.392	47.982	306	0.841	34.000	1.027404
LV-85	C6	05/23/2019	141.392	47.982	316	0.839	34.038	1.027435
LV-70	C6	06/19/2015	141.392	48.246	0	10.731	33.617	1.025903
LV-70	C6	06/19/2015	141.392	48.246	34	7.335	33.826	1.026598
LV-70	C6	06/19/2015	141.392	48.246	60	4.461	33.879	1.026998
LV-70	C6	06/19/2015	141.392	48.246	95	3.874	33.999	1.027154
LV-70	C6	06/19/2015	141.392	48.246	142	3.001	33.991	1.027232
LV-70	C6	06/19/2015	141.392	48.246	174	2.373	33.990	1.027286
LV-70	C6	06/19/2015	141.392	48.246	202	2.307	34.019	1.027314
LV-70	C6	06/19/2015	141.392	48.246	230	2.157	34.025	1.027331
LV-70	C6	06/19/2015	141.392	48.246	258	2.070	34.027	1.027339
LV-70	C6	06/19/2015	141.392	48.246	286	1.553	34.037	1.027387
LV-70	C6	06/19/2015	141.392	48.246	310	1.359	34.041	1.027404
LV-70	C6	06/19/2015	141.392	48.246	319	1.267	34.042	1.027411
Tatar Strait W. Slope References Site [1]								
LV85	C2	5/21/19	140.5895	48.20316	0	4.644	32.498	1.025882
LV85	C2	5/21/19	140.5895	48.20316	50	0.630	33.671	1.027154
LV85	C2	5/21/19	140.5895	48.20316	75	0.942	33.823	1.027257
LV85	C2	5/21/19	140.5895	48.20316	100	1.043	33.874	1.027291
LV85	C2	5/21/19	140.5895	48.20316	150	1.190	33.936	1.027331
LV85	C2	5/21/19	140.5895	48.20316	200	1.059	33.988	1.027381
LV85	C2	5/21/19	140.5895	48.20316	300	0.820	34.040	1.027439
LV85	C2	5/21/19	140.5895	48.20316	364	0.781	34.040	1.027441
LV85	C2	5/21/19	140.5895	48.20316	374	0.781	34.040	1.027441
Tatar Strait Slope and Trough [2]								
KH-35	124	07/28/1999	141.4400	48.0000	3.2	11.105	33.243	1.025548
KH-35	124	07/28/1999	141.4400	48.0000	66.3	2.2516	34.038	1.027334
KH-35	124	07/28/1999	141.4400	48.0000	111.7	1.8835	34.031	1.027358
KH-35	125	07/28/1999	141.0400	48.0000	4.2	11.793	33.089	1.025307
KH-35	125	07/28/1999	141.0400	48.0000	21.6	2.903	33.688	1.026999
KH-35	125	07/28/1999	141.0400	48.0000	40.0	1.289	33.825	1.027235
KH-35	125	07/28/1999	141.0400	48.0000	139.6	1.214	33.981	1.027366
KH-35	125	07/28/1999	141.0400	48.0000	254.4	1.251	34.076	1.027439
KH-35	125	07/28/1999	141.0400	48.0000	348.4	0.835	34.071	1.027463
KH-35	125	07/28/1999	141.0400	48.0000	441.9	0.606	34.070	1.027476
KH-35	125	07/28/1999	141.0400	48.0000	648.6	0.327	34.067	1.027490
KH-35	125	07/28/1999	141.0400	48.0000	801.0	0.233	34.065	1.027493
KH-35	125	07/28/1999	141.0400	48.0000	838.4	0.235	34.065	1.027493
KH-35	127	07/29/1999	140.7533	48.0000	3.6	12.100	32.945	1.025141
KH-35	127	07/29/1999	140.7533	48.0000	69.5	1.273	33.924	1.027316
KH-35	127	07/29/1999	140.7533	48.0000	160.5	0.669	33.968	1.027390
KH-35	127	07/29/1999	140.7533	48.0000	219	0.833	34.022	1.027424
KH-35	127	07/29/1999	140.7533	48.0000	268.5	0.718	34.042	1.027447
KH-35	127	07/29/1999	140.7533	48.0000	362.4	0.652	34.048	1.027456
KH-35	128	07/29/1999	140.4150	48.0017	28.9	1.0184	33.280	1.026815
KH-35	128	07/29/1999	140.4150	48.0017	59	0.2819	33.762	1.027246
KH-35	128	07/29/1999	140.4150	48.0017	116.9	0.6764	33.938	1.027365
Umitaka Spur, Niigata Prefecture [3]								
KT05-11	1D1-12	05/19/2005	137.33	41.35	300.63	1.3965	34.1551	1.027492
KT05-11	1D1-11	05/19/2005	137.33	41.35	499.63	0.6234	34.1704	1.027555
KT05-11	1D1-9	05/19/2005	137.33	41.35	720.3	0.3476	34.1707	1.027571
KT05-11	1D1-1	05/19/2005	137.33	41.35	911.29	0.2521	34.1689	1.027574

[1] This study, [2] Postlethwaite et al., 2005, and [3] Takahata et al., 2008; Saegusa et al., 2007.

TABLE 2 | Noble gas, methane, and dissolved inorganic carbon stable isotopic data for samples collected in Niskin bottles.

Cruise	Site	Depth (m)	$^3He/^4He$ (R/R_{air})	δ^3He (%)	$^{20}Ne/^4He$	$\Delta^{20}Ne/^4He$ (%)	CH_4 (nmol/L)	CH_4 SR (%)	$\delta^{13}C_{DIC}$ (‰)
Tatar Strait Slope Seeps [1]									
LV-85	C5	0	a.c.	a.c.	a.c.	a.c.	5.7	63.0	0.02
LV-85	C5	50	0.982 ± 0.01	−1.8	3.81	−3.48	13.2	245.6	−0.66
LV-85	C5	75	0.979 ± 0.01	−2.1	3.71	−6.14	31.4	728.8	−0.74
LV-85	C5	100	0.997 ± 0.01	−0.3	3.67	−6.93	31.5	740.6	−0.87
LV-85	C5	150	1.007 ± 0.01	0.7	3.58	−9.24	a.c.	a.c.	−0.86
LV-85	C5	200	1.001 ± 0.01	0.1	3.51	−11.16	145.8	3740.5	−0.86
LV-85	C5	250	1.023 ± 0.01	2.3	3.93	−0.61	42.7	1020.1	−0.96
LV-85	C5	326	1.035 ± 0.01	3.5	3.79	−4.22	35.7	834.8	−0.93
LV-85	C5	336	1.039 ± 0.01	3.9	3.75	−5.25	34.4	801.4	−1.05
LV-85	C6	0.15	0.984 ± 0.01	−1.6	3.72	−5.04	5.3	50.8	n.d.
LV-85	C6	40	0.988 ± 0.01	−1.2	3.96	−0.81	7.7	96.4	n.d.
LV-85	C6	75	0.991 ± 0.01	−0.9	3.94	−0.63	8.3	118.7	n.d.
LV-85	C6	100	0.989 ± 0.01	−1.1	4.00	1.30	8.4	126.2	n.d.
LV-85	C6	150	0.984 ± 0.01	−1.6	3.94	0.05	7.6	109.1	n.d.
LV-85	C6	200	0.97 ± 0.01	−3	3.67	−6.90	8.3	127.8	n.d.
LV-85	C6	250	1.022 ± 0.01	2.2	3.76	−4.76	14.7	299.0	n.d.
LV-85	C6	306	1.033 ± 0.01	3.3	3.76	−4.94	92.9	2386.2	n.d.
LV-85	C6	316	a.c.	a.c.	a.c.	a.c.	46.1	1134.6	n.d.
LV-70	6	0	n.d.	n.d.	n.d.	n.d.	11.1	301.1	n.d.
LV-70	6	34	n.d.	n.d.	n.d.	n.d.	29.4	879.3	n.d.
LV-70	6	60	n.d.	n.d.	n.d.	n.d.	172.0	5212.0	n.d.
LV-70	6	95	n.d.	n.d.	n.d.	n.d.	46.1	1303.6	n.d.
LV-70	6	142	n.d.	n.d.	n.d.	n.d.	26.5	687.3	n.d.
LV-70	6	174	n.d.	n.d.	n.d.	n.d.	17.0	396.7	n.d.
LV-70	6	202	n.d.	n.d.	n.d.	n.d.	29.4	758.3	n.d.
LV-70	6	230	n.d.	n.d.	n.d.	n.d.	24.0	596.4	n.d.
LV-70	6	258	n.d.	n.d.	n.d.	n.d.	24.1	597.9	n.d.
LV-70	6	286	n.d.	n.d.	n.d.	n.d.	30.8	777.6	n.d.
LV-70	6	310	n.d.	n.d.	n.d.	n.d.	23.9	577.8	n.d.
LV-70	6	319	n.d.	n.d.	n.d.	n.d.	121.5	3340.8	n.d.
Tatar Strait W. Slope References Site [1]									
LV85	C2	0	n.d.	n.d.	n.d.	n.d.	5.3	64.3	n.d.
LV85	C2	50	n.d.	n.d.	n.d.	n.d.	11.0	205.2	n.d.
LV85	C2	75	n.d.	n.d.	n.d.	n.d.	9.8	174.1	n.d.
LV85	C2	100	n.d.	n.d.	n.d.	n.d.	9.2	159.3	n.d.
LV85	C2	150	n.d.	n.d.	n.d.	n.d.	7.6	113.5	n.d.
LV85	C2	200	n.d.	n.d.	n.d.	n.d.	8.9	150.3	n.d.
LV85	C2	300	n.d.	n.d.	n.d.	n.d.	12.0	235.6	n.d.
LV85	C2	364	n.d.	n.d.	n.d.	n.d.	13.0	263.2	n.d.
LV85	C2	374	n.d.	n.d.	n.d.	n.d.	12.8	256.4	n.d.
Tatar Strait Slope and Trough [2]									
KH-35	125	4.2	0.9863	−1.4	a.c.	a.c.	n.d.	n.d.	n.d.
KH-35	125	21.6	0.9831	−1.7	4.02	2.53	n.d.	n.d.	n.d.
KH-35	125	40.0	n.d.	n.d.	n.d.	n.d.	n.d.	n.d.	n.d.
KH-35	125	139.6	0.9947	−0.5	4.03	2.05	n.d.	n.d.	n.d.
KH-35	125	254.4	1.0213	2.13	4.02	1.85	n.d.	n.d.	n.d.
KH-35	125	348.4	1.0443	4.43	4.03	1.76	n.d.	n.d.	n.d.
KH-35	125	441.9	1.07	7	4.05	2.10	n.d.	n.d.	n.d.
KH-35	125	648.6	n.d.	n.d.	n.d.	n.d.	n.d.	n.d.	n.d.
KH-35	125	801.0	1.0721	7.21	4.02	1.27	n.d.	n.d.	n.d.
KH-35	125	838.4	n.d.	n.d.	n.d.	n.d.	n.d.	n.d.	n.d.
KH-35	127	3.6	0.981	−1.9	3.71	−1.76	n.d.	n.d.	n.d.
KH-35	127	69.5	n.d.	n.d.	n.d.	n.d.	n.d.	n.d.	n.d.
KH-35	127	160.5	n.d.	nd.	n.d.	n.d.	n.d.	n.d.	n.d.
KH-35	127	219	1.0101	1.01	4.02	1.54	n.d.	n.d.	n.d.
KH-35	127	268.5	1.0261	2.61	4.02	1.40	n.d.	n.d.	n.d.
KH-35	127	362.4	1.0353	3.53	4.01	1.14	n.d.	n.d.	n.d.
Umitaka Spur, Niigata Prefecture [3]									
KT05-11	1D1-12	300.63	1.003	0.3	3.72	−5.84	6.3	79.1	n.d.
KT05-11	1D1-11	499.63	1.023	2.3	3.78	−4.47	23.1	543.3	n.d.
KT05-11	1D1-9	720.3	1.054	5.4	3.86	−2.77	3.5	−3.4	n.d.
KT05-11	1D1-1	911.29	1.045	4.5	3.86	−2.72	5.6	54.1	n.d.

[1] This study, [2] Postlethwaite et al., 2005, and [3] Takahata et al., 2008; Saegusa et al., 2007. n.d.= not determined, a.c.= air-contaminated sample split.

determined coefficients (Smith and Kennedy, 1983; Sano and Takahata, 2005) as well as with the temperatures and salinity shown in **Figures 7A,B** along with the $^{20}Ne/^{4}He$ ratio measured from waters collected from the Niskin bottles (**Table 2**).

Using this approach, it can be seen (**Figure 7G**) that for the Tatar Strait samples collected in 1999 (KR125 and KR127), only surface waters present negative $\Delta^{20}Ne/^{4}He$ values, meaning that the waters are undersaturated in ^{20}Ne relative to ^{4}He, at the given temperature and salinity conditions. All of the other samples collected in 1999 are above saturation for neon relative to helium. In contrast, during 2019, the $\Delta^{20}Ne/^{4}He$ values for plume LV85-seepC5 are negative for both surface (I) and subsurface (II) waters, decreasing almost linearly with depth to the base of the lower intermediate waters (IIIb) and then increasing somewhat for deeper Japan Sea Proper (IV) samples. The $\Delta^{20}Ne/^{4}He$ profile for 2019 plume LV85-seepC6 similar to the 1999 profile, in that values are negative in the surface (I), then around saturation down to the base of lower intermediate (IIIb), with the exception of one negative value at the boundary between water layers IIIb and IV. At the depths of Japan Sea Proper (IV) water, the 2019 samples are not appreciably different from the Umitaka Spur samples from offshore Niigata Prefecture which also have negative $\Delta^{20}Ne/^{4}He$ values and only approach solubility near the seafloor. The very gradual changes in Umitaka Spur may be since the Umitaka Spur is in deeper water (>900 m), compared with the Tatar Strait plumes (<400 m). In the central portions of Japan Sea, the relative amount of neon the helium appears to increase more gradually as the transition between water masses is also deeper (Postlethwaite et al., 2005; Takahata et al., 2008).

Stable Isotopic Composition of DIC in Seawater at a Plume Site

The $\delta^{13}C$ of DIC was determined in seawater that was recovered and transferred from Niskin bottles above site LV85-seepC5 in 2019 (**Table 2**). The measured values begin slightly positive at +0.02‰ in the shallowest waters and become increasingly more depleted in ^{13}C with depth, with the deepest sample (336 m) having the most negative $\delta^{13}C$ value at −1.16‰. Although at 200 m depth, LV85-seepC5 has an anomalously low $\Delta^{20}Ne/^{4}He$ value (−11.6%) coupled with a very high methane oversaturation ratio (3740%), the $\delta^{13}C$ of DIC at this depth shows no such anomaly and is consistent with adjacent water samples at −0.86‰.

DISCUSSION

Presence and Fate of Methane at Plume Sites

Although to date there have not been ROV deployments to directly observe the seafloor seeps in Tatar Strait, the flares themselves (**Figure 3)** are thought to be comprised of free gas, free gas enclosed in a gas hydrate shell, or gas hydrate flakes similar to those observed elsewhere in related studies including at Umitaka Spur (Aoyama et al., 2007). In these cases, it has been shown that the ascending gas hydrate melts and gas bubbles disperse within the water column before reaching the subsurface (II) and surface (I) waters (e.g., Greinert et al., 2006; Salomatin et al., 2014). Gravity coring during both LV70 and LV85 as well as the previous cruises has revealed thin laminar gas hydrate layers in the shallow sediments beneath the plumes (Jin et al., 2013; Shakirov et al., 2019), while no sediment-hosted gas hydrate has been recovered from the western margin of Tatar Strait where the reference site LV85-C2ref. is located.

The Tatar Strait plumes differ from plumes situated offshore of NE Sakhalin (Salomatin et al., 2014) and Umitaka Spur (Aoyama et al., 2007) in that the location of gas venting in Tatar Strait is significantly shallower. Plumes at Umitaka Spur, Sea of Japan (**Figure 1A**) are at 900 m or more (Aoyama et al., 2007; Hiruta et al., 2015), while numerous plumes situated in the Okhotsk Sea to the northeast of Sakhalin Island are mostly found between 500 and 1000 m (Jin et al., 2011). Any gas hydrate forming at 350 m at the base of the Tatar Strait Plumes, would travel a much shorter distance before dissociating and dissipating into the water column. The speed of ascending bubbles decreases as the diameter of the bubbles becomes smaller until they eventually reach neutral buoyancy and dissipate in the water column (Yapa et al., 2001; Greinert et al., 2006; Salomatin et al., 2014). Assuming an average vertical velocity of 15 cm/s (Salomatin et al., 2014) bubbles could presumably travel up to 100 m depth in as little as 28 min. On the other hand, at such shallow depths, the water pressure is less at the top of upper intermediate waters (IIIa), which leads to more rapid dissociation of gas hydrate and dissipation into the water column. In any case, the echograms would suggest that most of what is free gas has dissipated into the water column in the intermediate waters (IIIa and IIIb) or at least reached a bubble diameter so small that it cannot be detected through hydroacoustic methods.

If the most intense red and orange areas within the hydroacoustic flares (**Figure 3)** do in fact represent such gas hydrate which forms layers around rising gas bubbles as has been observed elsewhere in the Japan Sea (Aoyama et al., 2007), it is clear that the gas hydrate bubbles could extend into lower intermediate (IIIb) and even upper intermediate (IIIa) water masses, above the predicted range of gas hydrate stability (**Figure 7A**) as calculated from the equation of Dickens and Quinby-Hunt (1994). Shakirov et al. (2019) interpreted some of the shallower gas anomalies as being due to the dissociation gas hydrate bubbles, based on observations by Yapa et al. (2001), whereby gas hydrate from seeps which are relatively rich in ethane and propane, with $C_1/(C_2+C_3)<6$, can remain stable at higher temperatures and shallower depths, even shallower than intermediate waters (IIIa and IIIb) found in Tatar Strait. Recovered shallow seafloor sediments near the plume sites in Tatar Strait yield headspace gases which are primarily thermogenic with measured $C_1/(C_2+C_3)$ ratios <10 and as low as 2.8 (Yatsuk et al., 2020), so the upper limit of hydrate stability could potentially be shallower than the ~300 m depth indicated by pure methane, although the rising gas bubbles would have to be collected and analyzed to directly confirm this. It is apparent, however, that the presence of gas bubbles in the plume sites does not seem to have a detectible net effect on salinity or temperature

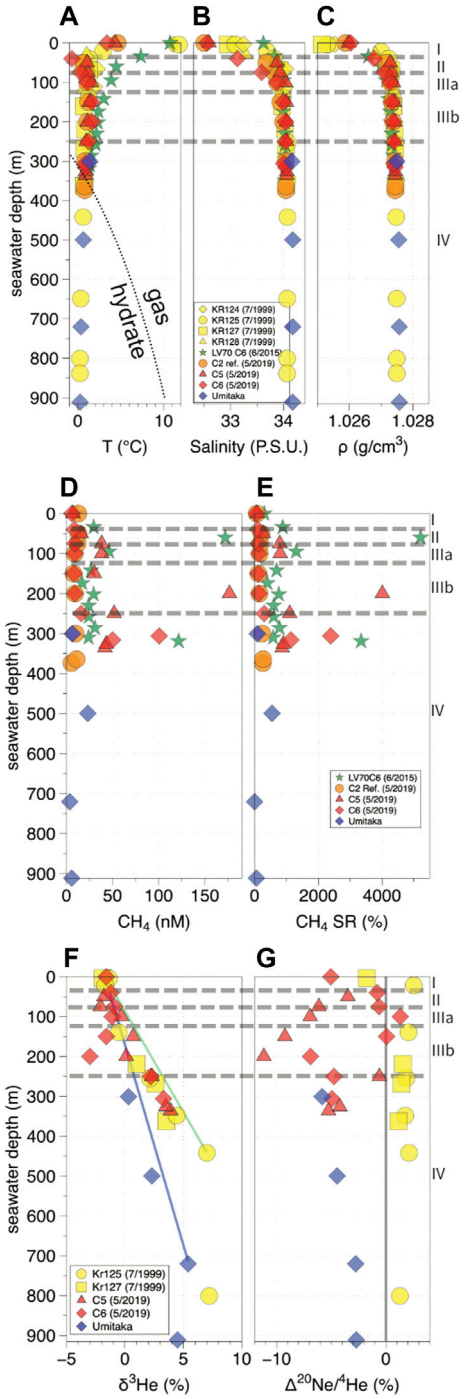

FIGURE 7 | (A,B) Depth profiles for temperature and salinity in seawater, respectively, from CTD data. Red represents plume samples from LV85-seepC5 and LC85-seepC6 in 2019, green stars represents plume LV70-seepC6 in 2015, yellow represents Tatar Strait sites from Cruise KH76 in 1999 (Postlethwaite et al., 2005), blue represents Umitaka Spur seep, offshore Niigata from Cruise KT05-11 in 2005 (Takahata et al., 2008). The dotted line shows gas hydrate stability for pure methane in seawater (Dickens and Quinby-Hunt, 1994) **(C)** Seater density calculated from temperature, salinity, and pressure (after UNESCO, 1981). **(D)** Dissolved methane. **(E)** Dissolved methane expressed as the oversaturation ratio (SR) calculated from

(*Continued*)

FIGURE 7 | concentration, temperature, and salinity. **(F)** Tritiogenic ^{3}He should increase somewhat linearly down to the base of intermediate waters (Postlethwaite et al., 2005). The slope is greater in Tatar Strait (green line) than that in Umitaka Spur due to Tatar Strait's shallower seafloor depth. Introduction of radiogenic ^{4}He in the plume sites at ~200 m water depth may be the cause of the apparent negative excursion in δ^{3}He. **(G)** Depth profile for Δ^{20}Ne/^{4}He calculated from the observed ratios, temperature, and salinity.

that influences the density (**Figure 7C**), as the profile from the reference site LV85-C2ref. is indistinguishable from the plume sites, nor are the Tatar Strait density profiles from the 1999 Tatar Strait transect sites observably different from the 2015 and 2019 plume sites.

In terms of CH_4 saturation in the water column, water collected from site LV85-C2ref. has the highest oversaturation in the deep Japan Sea Proper water (IV), decreasing only gradually until the base of surface water (I). The plume sites have high methane anomalies in the subsurface (II) and in lower intermediate water (IIIb). Such anomalies could potentially be from dissolved gas or from finely suspended gas bubbles entrained in the Niskin bottle at the time of sampling since the Niskin Rosette system passed directly into the plume during sampling (**Figure 3**). It is worth noting that, although accumulation of small gas bubbles at water mass boundaries is not impossible, the SSL observed in the hydrograms are probably not directly related to the gas seeps themselves, especially since similar SSL are also observed in the reference site (**Figure 3D**). Such SSL are frequently associated with the presence of zooplankton and micronekton in the water column (Liao et al., 1999) and, in such cases, position of the SSL often ascends during night time as these organisms tend to migrate closer to the surface (Evans and Hopkins, 1981; Baliño and Aksnes, 1993; Iida et al., 1996). Both the LV85-seepC6 (**Figure 3A**) and LV70-seepC6 (**Figure 3C**) were sampled during daylight hours (from 8:53 to 9:14 and from 6:47 to 7:09 local Sakhalin Time, respectively). During these hours, it seems that the SSL is most intense in surface (I) and subsurface (II) water layers, with hardly any reflection in the upper intermediate waters (IIIa) and a more broadly dispersed SSL in the lower intermediate waters (IIIb). In contrast, the CTD sampling and hydroacoustic measurements above plume LV85-seepC5 (**Figure 3B**) occurred at night (from 00:15 to 00:38). At the night time, the strong SSL is in the upper surface waters (I), while the more disperse SSL has migrated up from its position in the lower intermediate waters during daylight hours to upper intermediate (IIIa) and subsurface (II) waters. The reference site LV85-C2ref. was also sampled in the earlier night hours (from 21:02 to 21:34), yet with the exception of the surface waters (I), any deeper SSL is either absent for far more disperse than near the plume sites. While finely dispersed gas bubbles could potentially produce SSLs, these layers appear to change position between day and night and are likely entirely due to biotic activity.

Hydroacoustic data suggest that by the time the plume gas reaches the subsurface waters, the bubbles are dispersed enough that either the bubble diameter is too small for them to be

detected or they have dissolved into the surrounding water. Despite the disappearance from the hydrograms (**Figure 3**), the seawater methane in Tatar Strait is not completely oxidized; however, as shown by oversaturation ratios in surface (I) and subsurface (II) waters above both plumes and in the reference site (**Figure 3D**). If the gas dispersed from the plumes is effectively oxidized within the water column before reaching the air–water interface, it is possible that the oxidized methane would influence the carbon pool, at least around the plumes.

Unfortunately, with the exception of this plume study, there have not been other investigations of the $\delta^{13}C$ of DIC in the water column in Tatar Strait, or even in the Japan Sea to compare with at the time of this study. It is obvious from the data, however, that the more negative trend in $\delta^{13}C_{DIC}$ with depth observed at the Tatar Strait plume site is not caused by deep-water ventilation of sub-arctic, less saline Amur River water, even though rivers in other Arctic marginal sea settings have been shown to impart negative $\delta^{13}C_{DIC}$ values (Bauch et al., 2015; Dubinina et al., 2020). Such ventilation would require the Tatar Strait intermediate (IIIa, IIIb) and deep (IV) waters to be much less saline, less dense, and would have lower $\delta^{3}He$ values than those which are observed. To provide some comparison, the LV85-seepC5 results are plotted alongside with two reference sites where waters were also collected during late spring and early summer months along ocean margins where the water depth is similar, Skagerrak between the North Sea and the Baltic Sea (sampled in 5/19/2006) (Filipsson et al., 2017) and a shallow portion of the South China Sea (site-n, sampled during 6/1995) (Lin et al., 1999). For LV85-seepC5, the values generally become more negative with depth and with water density (**Figure 8A**). The largest difference is between surface (0 m, $\delta^{13}C_{DIC}$=+0.02‰) and subsurface (50 m, $\delta^{13}C_{DIC}$ = −0.66‰), and the most negative value is near the seafloor (336 m, $\delta^{13}C_{DIC}$ = −1.05‰). The waters of South China Sea (Lin et al., 1999) show a similar trend; however, the waters there show more positive $\delta^{13}C_{DIC}$ values and the water is significantly warmer (26.76 ˚C at 10 m to 34.46 ˚C at 301 m), leading to lower water density. Skagerrak samples show a more complex pattern since sub-surface waters are much shallower at <20 m consist of colder, less saline Baltic Sea waters which transition abruptly to more saline, warmer intermediate waters at only 50 m (Filipsson et al., 2017). That said, all of the Skagerrak waters have more positive $\delta^{13}C_{DIC}$ values than those of the Tatar Strait plume. There are some marine settings where the range of $\delta^{13}C_{DIC}$ values overlaps with those of the Tatar Strait site. A number of sites in the South China Sea (Lin et al., 1999) have $\delta^{13}C_{DIC}$ values which extend from around +1‰ in surface waters to just less than −1‰ in the deep waters; however, the more negative values are generally much deeper, at 500–1500 m depth. Bornholm Basin, Baltic Sea, has $\delta^{13}C_{DIC}$ values ranging from as high as +1.3‰ in surface waters to as low as −3.3‰ at 90 m (Filipsson et al., 2017); but the waters are less saline and less dense than those of Tatar Strait.

Depending on gas flux, the deep Japan Sea Proper (IV) water above the Tatar Strait gas plumes can possibly be influenced by the expulsion of fluids from gas vents. Sediment pore waters associated with seafloor gas chimneys have been shown to have quite negative $\delta^{13}C_{DIC}$ values of around −40‰ due primarily to anaerobic methane oxidation (Hiruta et al., 2015). We can see for example, that the deepest waters in plume LV85-seepC5 which are least influenced by tritiogenic ^{3}He are also those that have the

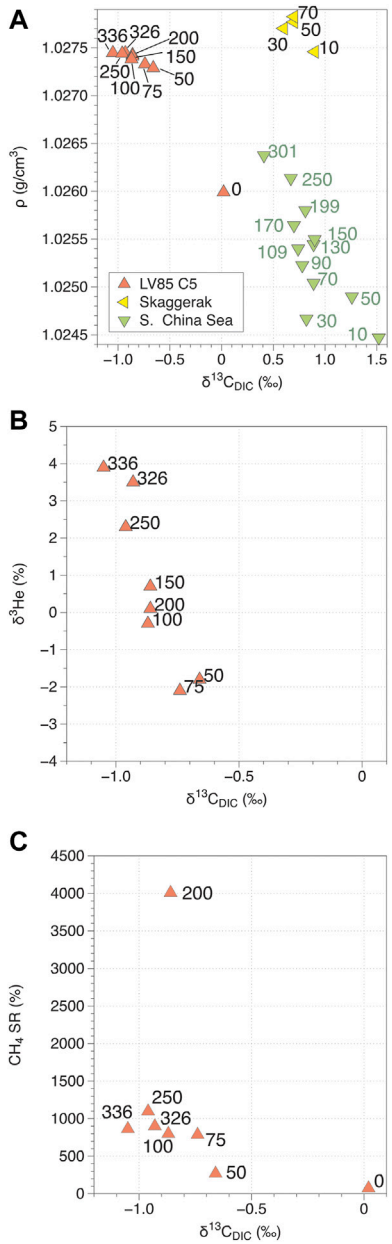

FIGURE 8 | Stable isotopic composition of dissolved inorganic carbon (DIC) versus gas composition at the LV85-seepC5 sampled in 5/2019. Depth indicated in meters beside each data point. **(A)** Deeper, dense waters generally have the most negative $\delta^{13}C$ values for DIC, compared to the South China Sea (Lin et al., 1999) and Skagerrak (Filipsson et al., 2017). **(B)** Most positive $\delta^{3}He$ values for LV85-seepC5 sampled in 2019 generally correspond with the deeper waters due to past tritiogenic production of ^{3}He in the waters, which also show an influence of DIC production from methane oxidation near the seafloor. **(C)** With the exception of the extremely high methane concentration at 200 m, there is generally more negative $\delta^{13}C$ with greater methane concentration in waters closer to the seafloor.

most negative $\delta^{13}C_{DIC}$ values (**Figure 8B**) and also that, with the deep Japan Sea Proper (IV) water with more negative $\delta^{13}C_{DIC}$ values also has a methane saturation ratio which is greater than the shallower surface (I) and subsurface (II) waters (**Figure 8C**). The problem is that contributions of DIC produced through mineralization of particulate organic matter as it settles on the seafloor can also impart negative $\delta^{13}C_{DIC}$ values similar to those observed. As such, the present data from the Tatar Strait plume is insufficient to determine whether the trend towards more negative values in the deep waters is influenced at all by the localized expulsion of water from a single gas chimney or even from fluids expelled by multiple gas seeps on a more regional scale. Future studies of the $\delta^{13}C_{DIC}$ in this area are merited. In a recent study, Na et al. (2022) found that the DIC concentrations in deep Japan Sea waters have increased significantly between 1999 and 2019, due to the slowing of ventilation of shallow waters coupled with an increasing contribution of DIC from oxidation of detrital material. Since an increase in dissolved CO_2 from oxidation of particulate organic carbon can lead to deep water acidification, clearly more research is needed to see if this is occurring in Tatar Strait.

Another environmental concern in light of the global warming potential of methane gas is the transfer of methane from shallow surface waters (I) to the atmosphere. The methane flux into the atmosphere from the shallow ocean can be calculated as follows (Kudo et al., 2018):

$$F_{CH4} = K_w \text{ x } ([CH_4]_{w(0-10m)} - [CH4]_a), \quad [7]$$

where F_{CH4} is the flux in μmol/m^2/day (also reported in some studies as mol/km^2/day), K_w is the gas transfer coefficient in cm/hr, $[CH_4]_{w(0-10m)}$ is the concentration of methane in μmol/L in the upper 10 m of water depth, and $[CH_4]_a$ is the saturation concentration of atmospheric methane in water from **Eq. 3.** The gas transfer coefficient (K_w) is calculated as follows:

$$K_w = 0.31v^2 (Sc/660)^{-1/2}, \quad [8]$$

where v is the wind speed in m/s and S_c is the Schmidt number for CH_4 in seawater. The Schmidt number which is dimensionless is calculated as follows:

$$Sc = 2039.2 - 120.31T + 3.4029T^2 - 0.040437T^3, \quad [9]$$

where T in this case is temperature in °C. As can be appreciated in **Eq. 8**, changes in wind speed have a strong influence on the gas transfer coefficient which is directly proportional to the flux of methane to the atmosphere, more than air temperature change. The range of wind velocities measured during sampling of the plumes and the reference site during cruise LV85 ranged from 1.1 to 7.7 m/s, while air temperature varied from 5.2 to 7.9 °C. In another study, wind velocities measured during a sampling in the southernmost portion of Tatar Strait in August, 2010 yielded a range from 2 to 10 m/s (Vereschchagina et al., 2013). In order to provide a meaningful comparison of methane flux between the plume sites and the reference site regardless of changes in weather, we assume a constant air speed of 7 m/s and an air temperature of 6 °C, yielding a Schmidt number (S_c) of 1431 and a gas transfer coefficient (K_w) of 10.32 cm/h. The gas transfer coefficient is then applied to the difference in measured concentrations of methane observed in shallow waters versus the calculated air saturation values yielding flux values for the plume sites and the reference site (**Supplementary Table S1**). The 2019 reference site LV85-C2ref has a methane flux of 5.16 μmol/m^2/day. Despite having much higher methane concentrations in the intermediate waters, the two plume sites from the same year, LV85-seepC6 and LV85-seepC5 have essentially the same flux to the atmosphere at 4.41 μmol/m^2/day and 5.18 μmol/m^2/day, respectively. The 2015 site LV70-seepC6 has an atmospheric methane flux which is significantly greater, at 20.68 μmol/m^2/day. It is also possible that sporadic gas emissions can result in even greater methane emissions, as noted with an anomalously high methane profile for 2015 site LV70-20, which has near-surface concentrations of 115 nmol/L and yields an atmospheric flux of 482 μmol/m^2/day (Shakirov et al., 2019). It could be that some the methane fluxes are variable from year to year as noted by Mishukova et al. (2015), in part as a result of sporadic releases of gas following local seismic activity (Shakirov et al., 2020). Although there was no significant difference between plume and reference sites in sampled during LV85 in 2019, all of the calculated fluxes are higher than those of non-plume sites to the south of Tatar Strait which were shown to range from 0.1 μmol/m^2/day to 0.6 μmol/m^2/day using a similar method of calculation (Vereshchagina et al., 2013). Aoki et al. (2020) demonstrated that methane concentrations in the air just above the sea surface in Umitaka Spur were significantly greater than background atmospheric values in other parts of Japan Sea. It could be that the calculated plume values for Tatar Strait are an underestimate, if plume gases dispersing and entering over a larger area, or if the plume gas is moving laterally beyond our sampling area before reaching the surface.

Mixing of Water Masses and Temporal Changes

In general, combining the observed chemical and isotopic results suggest three different groups based on mixing trends between the described water masses (**Figure 2**) as shown by on cross plots with the water depth noted alongside the data (**Figure 9**). The theoretical $^{20}Ne/^4He$ ratios (calculated form Sano and Takahata, 2005; Smith and Kennedy, 1983) are only slightly influenced by the observed range of salinities (green lines), with predicted ratios for 0 °C representing the coldest waters versus 15 °C representing the warmest summer temperatures in southern Tatar Strait (Andreev, 2018). Group-a comprises all the samples deeper than 150 m from July, 1999 (Postlethwaite et al., 2005) from lower intermediate waters (IIIb), as well as possibly one of the deeper 2019 samples. This group represents mixing of the lower intermediate waters (IIIb) with cold deep Japan Sea Proper waters (IV), all with salinities all between 34.0 and 34.1 PSU. Group-b occurs at <150 m deep and represents mixing between less saline surface waters (I) and subarctic subsurface water masses (II) and as well as the upper portion of Intermediate low-salinity water

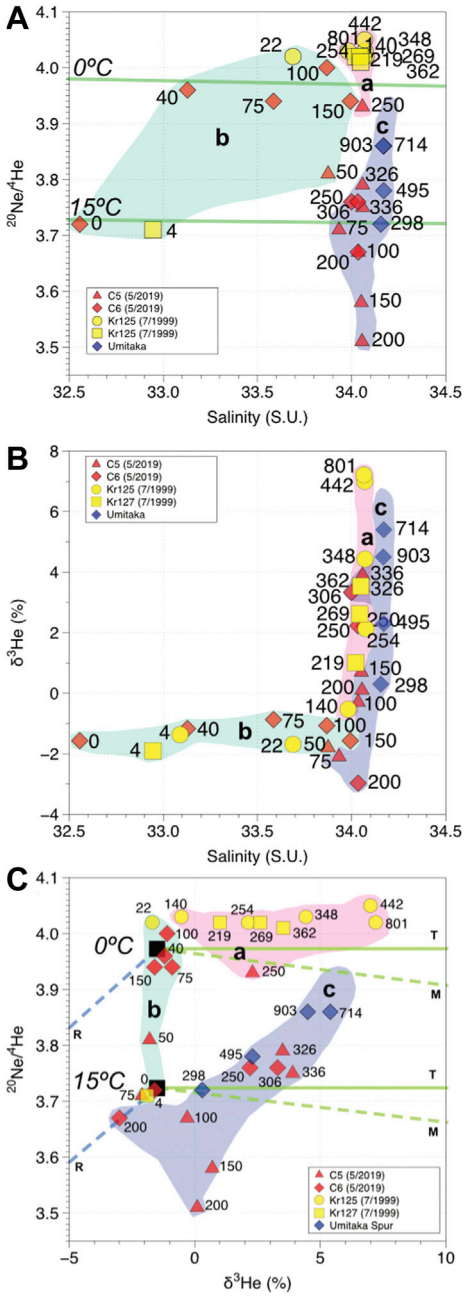

FIGURE 9 | Mixing trends observed in Tatar Strait and Umitaka Spur water masses. Seawater depth indicated in meters. **Group-a:** Mixing between subarctic intermediate and deep waters. **Group-b:** Mixing between less saline surface waters and subarctic subsurface waters **Group-c:** Mixing slightly more saline subtropical intermediate and deep waters. **(A)** Observed salinities have only a modest effect on $^{20}Ne/^{4}He$ ratios, as shown by the solubility lines (green) at 0 and 15 °C. As shown, low salinity values are mostly shallow waters. Extremely low values for $^{20}Ne/^{4}He$ can be produced either by air injection or by the addition of radiogenic ^{4}He. **(B)** Salinity versus $\delta^{3}He$. Low salinity values are primarily from surface and subsurface Group-b. **(C)** Addition of mantle gas (M) appear to be minimal, and mixing of tritiogenic (T) ^{3}He in intermediate and deep waters seems to be the source of the observed variation. Points below and to the left of the 15 °C seawater end-member indicate some modification of group III by the addition of radiogenic

(*Continued*)

FIGURE 9 | helium, particularly in intermediate waters at around 200 m. The 1999 waters tend to trend between intermediate and deep sub-arctic values in Group-a while the Umitaka Spur and Tatar 2019 waters show an influence form the Tsushima Current sub-tropical waters, particularly in the intermediate water masses.

masses (IIIa). Members of this group are represented by samples from both July, 1999 and May, 2019. The warmer, less saline portion of Group-b is restricted to <4 m and may represent low-salinity subarctic waters that have warmed during the spring to mid-summer months. Finally, Group-c represents the mixing between more-saline subtropical intermediate waters (IIIb) with anomalously low $^{20}Ne/^{4}He$ ratios and deep Japan Sea Proper waters (IV). This group includes seawater sampled in May, 2019 as well as the Umitaka Spur samples. Roughly half of the samples in this group have anomalous $^{20}Ne/^{4}He$ ratios which cannot be accounted for by air saturation even at temperatures above the warmest water temperatures of 15 °C, especially since the actual water temperatures are much lower.

Looking at the $\delta^{3}He$ values for the same samples involved in the aforementioned groups (**Figure 9B**) reveals some more details. While Group-a does not very much in $^{20}Ne/^{4}He$ ratios, it spans a wide range of $\delta^{3}He$ values which increase predictably with water depth. Group-b, however, has a limited range of $\delta^{3}He$ values, since these surface and subsurface waters are not influenced by tritiogenic ^{3}He from the early to mid-1960's. Group-c waters are more saline than Group-a, but also have increasing $\delta^{3}He$ values with depth. Some of the $\delta^{3}He$ values for waters involved in Group-c are even lower than those of the shallow waters.

Finally, combining the $\delta^{3}He$ values with $^{20}Ne/^{4}He$ values (after Takahata et al., 2005), we can also consider mixing of warm and cold waters with several other gas sources (**Figure 9C**). Addition of tritiogenic helium (T) would increase the $\delta^{3}He$ values while having no effect on $^{20}Ne/^{4}He$ (solid green lines). Addition of even minor amounts of mantle helium (M) would cause a large increase in $\delta^{3}He$ with a corresponding drop in $^{20}Ne/^{4}He$ (dashed green lines). Addition of a radiogenic ^{4}He component (R) would cause both $\delta^{3}He$ values and $^{20}Ne/^{4}He$ ratios to drop (dashed blue lines). Considering this, Group-a consists of cold waters with varying degrees of tritiogenic ^{3}He addition which increases with depth. It is not entirely clear why the $^{20}Ne/^{4}He$ ratios are above seawater saturation, though. The formation of ice during the winter months could possibly increase the relative amount of He sequestered in ice bubbles, with injection of cold dense brines produced by the freezing of seawater resulting in intermediate and deep waters with higher $^{20}Ne/^{4}He$ ratios (Hamme and Emerson, 2002; Hamme et al., 2019). Group-b consists of shallow waters which are free of tritiogenic ^{3}He.

This group covers a large range of salinities depending on the relative amount of water from the Tsushima and Amur River currents. While there is a large amount of variation in $^{20}Ne/^{4}He$ ratios, this could also be the result of changes in the

relative solubility of neon and helium entirely due to temperature differences. Group-c includes intermediate to deep waters which are enriched, in varying degrees, with tritiogenic ^{3}He, but which have lower ^{20}Ne/^{4}He ratios than Group-a. Only two samples from May 2019, at 75 and 200 m, have negative δ^{3}He values, suggesting potential mixing between shallow warm waters and a crustal radiogenic ^{4}He source that could have originated from the gas plume. While gas associated with methane hydrate in Umitaka Spur has mantle helium (^{3}He/^{4}He >2 R_a), radiogenic helium (^{3}He/^{4}He<0.1 R_a) has been found associated with gas hydrate in Lake Baikal, Russia (Matveeva et al., 2003) The other samples in this group at 100 m, 150 m, and 200 m do not fall on the radiogenic mixing trend, have atmospheric δ^{3}He values and could represent deeply advected air bubbles produced during ice formation and salt exclusion. This is not likely due to a problem during sample recovery, since the LV85-seepC5 samples appear to show a systematic decrease in ^{20}Ne/^{4}He with increasing depth between 50 and 200 m (**Figure 7G**). Hahm et al. (2004) observed a similar situation at Knipovich Ridge and proposed that such helium and neon anomalies are a combined effect of air bubble inclusions and brine injection caused by the process of salt exclusion which occurs during winter sea-ice formation. The phenomenon of deep convection of brines has been observed elsewhere in Japan, in particular in the southern Tatar Strait and offshore Primorye (Talley et al., 2003). In the case of Group-c waters, the ^{20}Ne/^{4}He ratios are lower than could reasonably be assumed through seawater saturation, yet are not as low as that of air (^{20}Ne/^{4}He$_{air}$= 3.14, Sakamoto et al., 1992). This would suggest brine injection into deep waters with air bubbles which have preferentially lost some of their helium due to ice formation. The most helium-depleted of Group-c waters are all >200 m depth and have both δ^{3}He values and ^{20}Ne/^{4}He ratios which approach the deeper waters observed in Group-a, while the least helium-depleted waters are <200 m and have δ^{3}He and ^{20}Ne/^{4}He ratios approaching those of air bubbles.

Potential for Climatic Fluctuations to Produce Significant Temporal Changes in Tatar Strait circulation

There are concerns that a decrease in deep water ventilation over the past two decades has already resulted in an increase in deep water acidification in the Japan Sea (Na et al., 2022) and it is also worrisome that changes in circulation may also decrease the upwelling of nutrient-rich waters (Jenkins, 2008) as well as changes in marine species distribution. Tatar Strait is relatively shallow when compared to the Japan Sea as a whole so the potential for significant change is even greater. Annual fluctuations in circulation appear to be intimately associated with the rate at which the Amur River discharges into the Okhotsk Sea across from the northernmost part of Sakhalin Island, and then spills over into Tatar Strait, thus influencing the northward migration of the Tsushima Current, and impacting both the thermohaline structure and circulation of water in the strait (Andreev, 2018; Ponomarev et al., 2018). As the Amur River is one of the largest rivers in East Asia, it has been hypothesized that increased water usage by humans as it courses through Mongolia, China, and Russia might lead to unintended changes in the thermohaline structure of Tatar Strait (Shevchenko et al., 2011).

To assess the degree to which riverine discharge may have varied over time, we looked hydrological data provided by the Russian Federal Water Resources agency for Brodgoroskoye, located at the mouth of the Amur River (**Figure 10**, **Supplementary Table S2**). The data shows average seasonal discharge during the period of Spring thaw each year (March, April, May) and the period of Fall monsoons (September, October, November). The data represents averages each season between 1990 and 2019, except for 2005–2007 where no data is available. With only one exception, the Spring discharge is less than that of the Fall discharge of the preceding year. The Spring discharge has increased only in the past decade but interannual variability has not changed appreciably. From 1990–1999, the mean and standard deviation of Spring discharge was 17,790 ± 3,500 m^3/s compared to the period of 2010–2019 where it was at 23,870 ± 3,800 m^3/s, representing an increase of 25%. If we compare Fall monsoonal discharge, both the mean and variability have increased from 33,200 ± 7,240 m^3/s from 1990–1999 to 52,990 ± 21,540 m^3/s, up by 37%. In general, we do not see a decreasing trend over time which would be attributable to increased water consumption through human activities as proposed by Shevchenko et al. (2011) and if water usage is increasing, it is more than offset by other factors which increase discharge. As far as possible changes in discharge related to intense weather activities, the most extreme seasonal discharge during this period (Fall, 2013: 97,300 m^3/s) is more than double that of the most extreme from 1990–1999 (Fall, 1994: 45,700 m^3/s).

The Fall monsoonal season of 2014, followed by the Spring thaw season of 2015 both preceded our sampling cruise in 2015 (LV70) and, compared with all of the other annual measurements of Amur River discharge, is unusual in that the Fall discharge is the second lowest for the decade (Shaded area in **Figure 10**) while the Spring discharge is the highest, resulting in the only year in which the Spring discharge is greater than that of the preceding Fall over a span of 30 years. This low Fall monsoonal discharge may have resulted in a decline in the intensity of the Amur Leeman and Primorye Currents (**Figure 1B**) and a northward encroachment of the warm saline Tsushima Current as described by Andreev (2018). In contrast, fall of 2018 marked the fourth highest monsoonal discharge for the decade, followed by the second lowest Spring discharge. The data for 1998–1999 and is in-between the extremes experienced in 2014–2015 and 2018–2019. These fluctuations in Amur River discharge could explain our CTD data for Tatar Strat shallow and subsurface water in 2015 is quite different from that 2019, and why the CTD data for 1999 is between the two (**Figure 4D**).

Regarding the influence of Amur River discharge on the Okhotsk Sea to the north, Ogi et al. (2001) found that the amount of ice cover in the Winter months was anticorrelated with the discharge rate recorded in the Fall monsoonal months of the previous year, presumably because of the transport of heat from the river water into the shallow surface layers of the Okhotsk. Subsequent research has further shown that annual

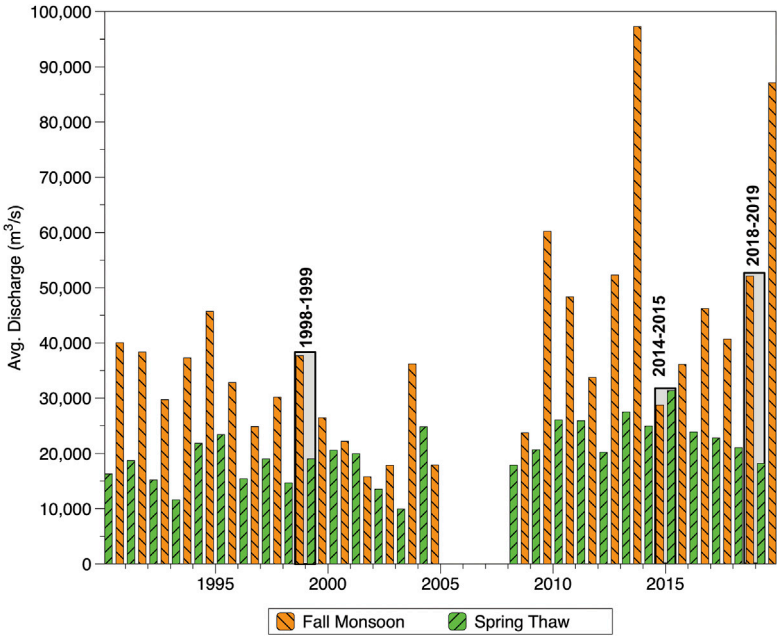

FIGURE 10 | Average seasonal discharge near the mouth of the Amur River in Brodgoroskoye. In general, between 2009 and 2018 the discharge is greater for both the spring thaw and the fall monsoonal months than between 1998 and 2005. The discharge was significantly lower during the fall of 2014 followed by only a slightly greater spring thaw discharge in 2015. (Data courtesy of the Russian Federal Water Resources Agency).

changes in Arctic Oscillation (AO) drive the fluctuations in humidity and Amur River Discharge which, in turn, influence shallow seawater temperatures and the extent of ice cover in the Okhotsk (Ogi and Tachibana, 2006).

Since the two extreme years of our study are 2015 and 2019, we compare Sentinel 1A Satellite imagery of the sea ice extent in Tatar Strait during the month of February in which we have shaded the thicker ice cover for greater visibility (**Supplementary Figure S3**). The rectangle indicating our study area in **Figure 1B** is also indicated in the supplementary figures and even though the images from the two years do not overlap exactly, the study area is present in both. In 2015, a year of low monsoonal input, the waters of the Amur are seen reducing the ice cover in the northern portions of the Strait (**Supplementary Figure S3A**) but their passage southward is blocked by ice restricting the circulation of shallow cold, freshwater southward by the Primorye Current along the western margin of Tatar Strait. At the same time, ice cover is reduced on eastern margin of the strait, along the shore of Sakhalin Island, due to the unimpeded northward flow of the Tsushima Current. With an ice-free area established in our study area in February, it is not surprising that the shallow waters observed in June were much warmer than other years. In contrast, during 2019, following high Fall monsoonal discharge, the western margin is in large part open to southward circulation of the Primorye Current, consistent with the anticorrelation between Amur River Discharge and ice extent in the Okhotsk Sea (Ogi et al., 2001; Ogi and Tachibana, 2006) yet impeding the northward migration of warm saline Tsushima Current waters to the east as described by Shevchenko et al., 2011, resulting in ice cover across most of our study area and along the coast of Sakhalin Island.

CONCLUSION

Our data is consistent with previous investigations which show that Amur River discharge appears to be a key factor in determining shallow, subsurface and even to some extent intermediate water circulation in the Tatar Strait since waters related to river discharge limit the extent to which the Tsushima Current can migrate northward along the coast of Sakhalin Island. Our noble gas results suggest that vertical migration of water masses is somewhat limited, since tritiogenic ^{3}He from the 1960's is still present in intermediate and deep waters. One concern has been that global warming has caused a slowing or even stopping of deep ventilation in the Tatar Strait since the 1960's and even more so in the past 20 years (Riser et al., 1999; Jenkins, 2008; Na et al., 2022), which would have profound implications regarding nutrient cycling and oxygen availability in parts of the water column. The presence of saline waters with low ^{20}Ne/^{4}He ratios and atmospheric δ^{3}He at depths of 100–250 m in 2019 would suggest that that is not entirely the case, and that deep convection as described by Talley et al. (2003), does still occur, perhaps even more so than the data of 1999 (Postlethwaite et al., 2005) when all the waters showed very high ^{20}Ne/^{4}He ratios. Unfortunately, our data is too limited in geographic distribution to tell if this is a localized phenomenon or whether it occurs more broadly. Since the Satellite images from the winters preceding the 2015 and 2019 sampling seasons show substantial changes in ice cover, one would expect that deep convection of air bubbles and brine also varies significantly from year to year depending on whether ice has accumulated more on the Primorye side of the Strait or on the Sakhalin Island side of the Strait.

Gas plumes, consisting primarily of methane gas, have been observed in deep and intermediate waters but are not visible in subsurface and surface waters. As has been noted by others (Shakirov et al., 2019, 2020), methane is still present in the water column in shallow water. The atmospheric flux observed in 2019 for plumes LV85-seepC5 and LV85-seepC6 (4.41 and 5.18 μmol/m^2/day, respectively) is essentially the same as that of the reference site LV85-C2ref. located on the opposite side of Tatar Trough (5.18 μmol/m^2/day), yet is significantly higher than values previously measured in the southernmost part of Tatar Strait (0.1–0.6 μmol/m^2/day Vereshchagina et al., 2013). The atmospheric flux that accompanied warm, saline surface and subsurface waters above the plumes in 2015 was greater at between 20.68 μmol/m^2/day observed at LV70-seepC6 (this study) and 684 μmol/m^2/day at LV70-20 (Shakirov et al., 2020). These flux values above the plumes may be underestimated due to lateral migration or more disperse transfer of the methane to the atmosphere.

As indicated by sites with similar depth profiles that are not associated with seeps, the stable isotopic composition of deep DIC seems to be affected in large degree by scavenging of CO_2 during shallow photosynthesis and by degradation of particulate organic matter in deep water. That said, more work should be done to monitor changes in DIC concentrations, $\delta^{13}C_{DIC}$, and as well as dissolved oxygen throughout the basin, in order to assess changes in water chemistry over the coming years.

While the noble gas isotopic data is limited to two seep sites from LV85 in 2019 as well as comparison with the published 1999 results from KH-36 (Postlethwaite et al., 2005), the observed depth profiles and notable differences in both δ^3He and Δ^{20}Ne/^{4}He from the two sampled years highlight the utility of noble isotope isotopic analysis in delimiting the interactions between water masses, and illustrate the necessity for more research which should be done in Tatar Strait, perhaps including tritium analyses of seawater in future cruises. In particular, future studies of air bubble injection due to brine rejection in winter months can indicate which parts of Tartar Strait undergo convection and whether the overall degree of deep ventilation in the strait is waning over time. Finally, ongoing research into marine seep sites should continue to focus on how methane plumes interact with local water masses and the degree to which plume activity contributes to greenhouse gas emissions.

DATA AVAILABILITY STATEMENT

The original contributions presented in the study are included in the article/**Supplementary Material**; further inquiries can be directed to the corresponding author.

AUTHOR CONTRIBUTIONS

GS: lead author, sample collection for noble gas analysis, data processing, and manuscript writing. AY: Niskin sample collection and gas concentration analysis. NT: noble gas isotopic analysis and manuscript revision. RS: research cruise lead investigator, site selection, and equipment planning. HT: equipment and sample shipping logistics and shipboard water chemistry. KT: analysis of stable isotopic composition of DIC. AO: research senior investigator, logistic planning, and site selection. AS: shipboard collection and analysis of hydroacoustic data. SA: shipboard sample preparation for land-based isotopic analysis and manuscript revision. EK: ice-cover analysis and interpretation of satellite data. EM: collection and analysis of CTD data. YS: noble gas analysis and manuscript revision. RM: lead investigator and organization of international research collaboration.

FUNDING

This research was carried out as part of a joint research program established between the Meiji University Gas Hydrate Research Laboratory (GHRL) and the Pacific Oceanological Institute Far Eastern Branch of Russian Academy of Sciences (POI FEB RAS). Marine expeditionary work was supported by the State Assignment of POI FEB RAS No. 0211-2021-0006 (121021500055-0) and approved by the Ministry of Science and Education of the Russian Federation.

ACKNOWLEDGMENTS

The authors would like to thank C. Postlethwaite for providing research data from the 1998–1999 study, the crew and researchers onboard the R/V Akademik M.A. Lavrentyev for their assistance in making the research cruise a success, and the reviewers who provided useful suggestions leading to the improvement of this manuscript.

SUPPLEMENTARY MATERIAL

The Supplementary Material for this article can be found online at: https://www.frontiersin.org/articles/10.3389/feart.2022.825679/full#supplementary-material

REFERENCES

Andreev, A. G. (2020). Impact of the Amur Discharge and Coastal Upwelling on the Water Circulation in the Northern Tartar Strait (Japan Sea). *Vestnik Far East Branch Russ. Acad. Sci.* 1, 120–126. (in Russian) http://www.vestnikdvo.ru/index.php/vestnikdvo/article/view/527.

Andreev, A. G. (2018). Peculiarities of Water Circulation in the Southern Tatar Strait. *Izv. Atmos. Ocean. Phys.* 54, 1050–1056. doi:10.1134/S0001433818090037

Aoki, S., Komiya, S., Oi, T., Noborio, K., and Matsumoto, R. (2020). Relationship between Atmospheric CH4 Concentration above Sea Surface and Gas Plumes from Seafloor along the Eastern Margin of Japan Sea and Around Hokkaido. *J. Jpn. Assoc. Petroleum Technol.* 85 (6), 309–314.

Aoyama, C., Matsumoto, R., Hiruta, A., Ishizaki, O., Machiyama, H., Numanami, H., et al. (2007). "Acoustical Surveys of Methane Plumes Using the Quantitative Echo Sounder in Japan Sea," in *Symposium on Underwater Technology and Workshop on Scientific Use of Submarine Cables and Related Technologie* (IEEE), 249–255. doi:10.1109/UT.2007.370804*s*

Atekwana, E. A., and Krishnamurthy, R. V. (1998). Seasonal Variations of Dissolved Inorganic Carbon and $\delta^{13}C$ of Surface Waters: Application of a Modified Gas Evolution Technique. *J. Hydrology* 205 (3–4), 265–278. doi:10.1016/S0022-1694(98)00080-8

Balino, B., and Aksnes, D. (1993). Winter Distribution and Migration of the Sound Scattering Layers, Zooplankton and Micronekton in Masfjorden, Western Norway. *Mar. Ecol. Prog. Ser.* 102, 35–50. doi:10.3354/meps102035

Bauch, D., Polyak, L., and Ortiz, J. D. (2015). A Baseline for the Vertical Distribution of the Stable Carbon Isotopes of Dissolved Inorganic Carbon (δ13CDIC) in the Arctic Ocean. *Arktos* 1 (1), 15. doi:10.1007/s41063-015-0001-0

Danchenkov, M. A. (2004). "Vladivostok: FERHRI)," in *Spatial Structure of the Tatar Strait Waters" in* Pacific Oceanography. Editor Y. N. Volkov, 2, 20–43.

Dickens, G. R., and Quinby-Hunt, M. S. (1994). Methane Hydrate Stability in Seawater. *Geophys. Res. Lett.* 21, 2115–2118. doi:10.1029/94GL01858

Dubinina, E. O., Kossova, S. A., Miroshnikov, A. Y., Avdeenko, A. S., and Chizhova, Y. N. (2020). Dissolved Inorganic Carbon ([DIC], δ13C(DIC)) in Waters of the Eastern East Siberian Sea. *Geochem. Int.* 58 (8), 867–886. doi:10.1134/S0016702920080054

Dulenina, P. A., Ustinova, E. I., and Dulenin, A. A. (2020). Current State of Resources for Japanese Flying Squid Todarodes Pacificus in the Northwestern Tatar Strait (Japan Sea). *Izv. Tihookean. Naučno-issled. Rybohoz. Cent.* 200 (3), 586–604. doi:10.26428/1606-9919-2020-200-586-604

Evans, R. A., and Hopkins, C. C. E. (1981). Distribution and Standing Stock of Zooplankton Sound-Scattering Layers along the North Norwegian Coast in February-March, 1978. *Sarsia* 66 (2), 147–160. doi:10.1080/00364827.1981.10414532

Filipsson, H. L., McCorkle, D. C., Mackensen, A., BernhardAndersson, J. M. L. S., Andersson, L. S., Naustvoll, L.-J., et al. (2017). Seasonal Variability of Stable Carbon Isotopes (δ13CDIC) in the Skagerrak and the Baltic Sea: Distinguishing between Mixing and Biological Productivity. *Palaeogeogr. Palaeoclimatol. Palaeoecol.* 483, 15–30. doi:10.1016/j.palaeo.2016.11.031

Gamo, T., Nakayama, N., Takahata, N., Sano, Y., Zhang, J., Yamazaki, E., et al. (2014). The Sea of Japan and its Unique Chemistry Revealed by Time-Series Observations over the Last 30 Years. *Monogr. Environ. Earth Planets* 2 (1), 1–22. doi:10.5047/meep.2014.00201.0001

Glorie, S., Alexandrov, I., Nixon, A., Jepson, G., Gillespie, J., and Jahn, B.-M. (2017). Thermal and Exhumation History of Sakhalin Island (Russia) Constrained by Apatite U-Pb and Fission Track Thermochronology. *J. Asian Earth Sci.* 143, 326–342. doi:10.1016/j.jseaes.2017.05.011

Greinert, J., Artemov, Y., Egorov, V., Debatist, M., and McGinnis, D. (2006). 1300-m-high Rising Bubbles from Mud Volcanoes at 2080m in the Black Sea: Hydroacoustic Characteristics and Temporal Variability. *Earth Planet. Sci. Lett.* 244 (1–2), 1–15. doi:10.1016/j.epsl.2006.02.011

Hahm, D., Postlethwaite, C. F., Tamaki, K., and Kim, K.-R. (2004). Mechanisms Controlling the Distribution of Helium and Neon in the Arctic Seas: the Case of the Knipovich Ridge. *Earth Planet. Sci. Lett.* 229 (1-2), 125–139. doi:10.1016/j.epsl.2004.10.028

Hamme, R. C., and Emerson, S. R. (2002). Mechanisms Controlling the Global Oceanic Distribution of the Inert Gases Argon, Nitrogen and Neon. *Geophys. Res. Lett.* 29 (23), 35-1–35-4. doi:10.1029/2002GL015273

Hamme, R. C., Nicholson, D. P., Jenkins, W. J., and Emerson, S. R. (2019). Using Noble Gases to Assess the Ocean's Carbon Pumps. *Annu. Rev. Mar. Sci.* 11 (1), 75–103. doi:10.1146/annurev-marine-121916-063604

Hiruta, A., Ishizaki, O., Tuchinaga, K., Snyder, G. T., and Matsumoto, R. (2015). Influence of the Carbon Isotopic Composition of Methane and the Proportion of Methane-Derived Bicarbonate on the 13C/12C Ratio of Dissolved Inorganic Carbon at the Sulfate-Methane Transition in the Joetsu Basin Area, Eastern Margin of the Sea of Japan. *Mar. Petroleum Geol.* 67, 468–480. doi:10.1016/j.marpetgeo.2015.05.004

Iida, K., Mukai, T., and DooJin, H. (1996). Relationship between Acoustic Backscattering Strength and Density of Zooplankton in the Sound-Scattering Layer. *ICES J. Mar. Sci.* 53 (2), 507–512. doi:10.1006/jmsc.1996.0073

IOC, IHOBODC (2003). "Centenary Edition of the GEBCO Digital Atlas," in *CD-ROM on Behalf of the Intergovernmental Oceanographic Commission and the International Hydrographic Organization* (Liverpool: British Oceanographic Data Centre). Published on www.gebco.net.

Jenkins, W. J. (2008). The Biogeochemical Consequences of Changing Ventilation in the Japan/East Sea. *Mar. Chem.* 108 (3-4), 137–147. doi:10.1016/j.marchem.2007.11.003

Jin, Y. K., Kim, Y.-G., Baranov, B., Shoji, H., and Obzhirov, A. (2011). Distribution and Expression of Gas Seeps in a Gas Hydrate Province of the Northeastern Sakhalin Continental Slope, Sea of Okhotsk. *Mar. Petroleum Geol.* 28 (10), 1844–1855. doi:10.1016/j.marpetgeo.2011.03.007

Jin, Y. K., Shoji, H., Obzhirov, A., Baranov, B., and R/V Akademik, M. A. (2013). "Operation Report of Sakhalin Gas Hydrate Project," in *Lavrentyev Cruise 59" Proceedings of SSGH-12* (Incheon: Korea Polar Research Institute).

Kawagucci, S., Ueno, Y., Takai, K., Toki, T., Ito, M., Inoue, K., et al. (2013). Geochemical Origin of Hydrothermal Fluid Methane in Sediment-Associated Fields and its Relevance to the Geographical Distribution of Whole Hydrothermal Circulation. *Chem. Geol.* 339, 213–225. doi:10.1016/j.chemgeo.2012.05.003

Kobayashi, M., Kouno, Y., Ito, M., Nishina, M., Fujimoto, Y., and Kato, K. (2009). "Seasonal Change in Number and Movement Pattern of Spotted Seals (*Phoca largha*) Migrating Around the Sea of Japan and Adjacent Areas," in *Paper Presented at Proceedings of the Fourth Workshop on the Okhotsk Sea and Adjacent Areas, Abashiri, Japan, August, 2008*. Editors M. Kashiwai and G. A. Kantakov (PICES Scientific Report No. 36), 76–81.

Kudo, K., Yamada, K., Toyoda, S., Yoshida, N., Sasano, D., Kosugi, N., et al. (2018). Spatial Distribution of Dissolved Methane and its Source in the Western Arctic Ocean. *J. Oceanogr.* 74, 305–317. doi:10.1007/s10872-017-0460-y

Lavrushin, V. Y., Polyak, B. G., Pyrazolo, R. M., and Kaminski, I. L. (1996). Sources of Material in Mud Volcano Products (Based on Isotopic, Hadrochemical, and Geological Data). *Lithology Mineral Resour.* 316, 557–578.

Liao, C., Lee, K. -T., Lee, M. -A., and Lu, H. -J. (1999). Biomass Distribution and Zooplankton Composition of the Sound-Scattering Layer in the Waters of Southern East China Sea. *ICES J. Mar. Sci.* 56, 766–778. doi:10.1006/jmsc.1999.0497

Lin, H.-L., Wang, L.-W., Wang, C.-H., and Gong, G.-C. (1999). Vertical Distribution of δ13C of Dissolved Inorganic Carbon in the Northeastern South China Sea. *Deep Sea Res. Part I Oceanogr. Res. Pap.* 46 (5), 757–775. doi:10.1016/S0967-0637(98)00091-0

Matveeva, T. V., Mazurenko, L. L., Soloviev, V. A., Klerkx, J., Kaulio, V. V., and Prasolov, E. M. (2003). Gas Hydrate Accumulation in the Subsurface Sediments of Lake Baikal (Eastern Siberia). *Geo-Marine Lett.* 23 (3-4), 289–299. doi:10.1007/s00367-003-0144-z

Mishukova, G. I., Mishukov, V. F., Obzhirov, A. I., Pestrikova, N. L., and Vereshchagina, O. F. (2015). Peculiarities of the Distribution of Methane Concentration and Methane Fluxes at the Water-Air Interface in the Tatar Strait of the Sea of Japan. *Russ. Meteorol. Hydrol.* 40, 427–433. doi:10.3103/S1068373915060096

Na, T., Hwang, J., Kim, S.-Y., Jeong, S., Rho, T., and Lee, T. (2022). Large Increase in Dissolved Inorganic Carbon in the East Sea (Japan Sea) from 1999 to 2019. *Front. Mar. Sci.* 9. doi:10.3389/fmars.2022.825206

Nicholson, D. P., Emerson, S. R., Khatiwala, S., and Hamme, R. C. (2011). "An Inverse Approach to Estimate Bubble-Mediated Air-Sea Gas Flux from Inert Gas Measurements," in *Proceedings on the 6th International Symposium on Gas Transfer at Water Surfaces*, 223–327. Available at: https://www.ldeo.columbia.edu/~spk/Papers/Nicholsonetal_InverseAirSeaFlux_11.pdf.

Ogi, M., and Tachibana, Y. (2006). Influence of the Annual Arctic Oscillation on the Negative Correlation between Okhotsk Sea Ice and Amur River Discharge. *Geophys. Res. Lett.* 33 (8). doi:10.1029/2006GL025838

Ogi, M., Tachibana, Y., Nishio, F., and Danchenkov, M. A. (2001). Does the Fresh Water Supply from the Amur River Flowing into the Sea of Okhotsk Affect Sea Ice Formation? *J. Meteorological Soc. Jpn.* 79 (1), 123–129. doi:10.2151/jmsj.79.123

Ogi, M., Taguchi, B., Honda, M., Barber, D. G., and Rysgaard, S. (2015). Summer-to-Winter Sea-Ice Linkage between the Arctic Ocean and the Okhotsk Sea through Atmospheric Circulation. *J. Clim.* 28 (12), 4971–4979. doi:10.1175/JCLI-D-14-00297.1

Park, K.-A., Kim, K., Cornillon, P. C., and Chung, J. Y. (2006). Relationship between Satellite-Observed Cold Water along the Primorye Coast and Sea Ice in the East Sea (The Sea of Japan). *Geophys. Res. Lett.* 33 (10), a–n. doi:10.1029/2005GL025611

Pishchal'nik, V. M., Arkhipkin, V. S., and Leonov, A. V. (2010). On Water Circulation in Tatar Strait. *Water Resour.* 37 (6), 759–772. doi:10.1134/S0097807810060035

Ponomarev, V. I., Fayman, P. A., Prants, S. V., Budyansky, M. V., and Uleysky, M. Y. (2018). Simulation of Mesoscale Circulation in the Tatar Strait of the Japan Sea. *Ocean. Model.* 126, 43–55. doi:10.1016/j.ocemod.2018.04.006

Postlethwaite, C. F., Rohling, E. J., Jenkins, W. J., and Walker, C. F. (2005). A Tracer Study of Ventilation in the Japan/East Sea. *Deep Sea Res. Part II Top. Stud. Oceanogr.* 52 (11-13), 1684–1704. doi:10.1016/j.dsr2.2004.07.032

Riser, S. C., Warner, M. J., and Yurasov, G. I. (1999). Circulation and Mixing of Water Masses of Tatar Strait and the Northwestern Boundary Region of the Japan Sea. *J. Oceanogr.* 55 (2), 133–156. doi:10.1023/A:1007881727369

R. Massel, S. (2015). "Internal Gravity Waves in the Shallow Seas," in *Internal Gravity Waves in the Shallow SeasGeoPlanet: Earth and Planetary Sciences*, 153–156. doi:10.1007/978-3-319-18908-6

Saegusa, S., Tsunogai, U., Nakagawa, F., Gamo, T., Zhang, J., Takeushi, A., et al. (2007). *Methane Anomalies in the Water Columns above Pockmarks, Offshore Sado Island*. Tokyo: Geochemical Society of Japan. Paper presented at Annual Meeting of the Geochemical Society of Japan 2005.

Sakamoto, M., Sano, Y., and Wakita, H. (1992). 3He/4He Ratio Distribution in and Around the Hakone Volcano. *Geochem. J.* 26 (4), 189–195. doi:10.2343/geochemj.26.189

Salomatin, A. S., Yusupov, V. I., Vereshchagina, O. F., and Chernykh, D. V. (2014). An Acoustic Estimate of Methane Concentration in a Water Column in Regions of Methane Bubble Release. *Acoust. Phys.* 60 (6), 671–677. doi:10.1134/S1063771014050133

Sano, Y., and Nakajima, J. (2008). Geographical Distribution of 3He/4He Ratios and Seismic Tomography in Japan. *Geochem. J.* 42 (1), 51–60. doi:10.2343/geochemj.42.51

Sano, Y., and Takahata, N. (2005). Measurement of Noble Gas Solubility in Seawater Using a Quadrupole Mass Spectrometer. *J. Oceanogr.* 61 (3), 465–473. doi:10.1007/s10872-005-0055-x

Shakirov, R. B., Syrbu, N. S., and Obzhirov, A. I. (2016). Distribution of Helium and Hydrogen in Sediments and Water on the Sakhalin Slope. *Lithol. Min. Resour.* 51 (1), 61–73. doi:10.1134/S0024490216010065

Shakirov, R. B., Valitov, M. G., Obzhirov, A. I., Mishukov, V. F., Yatsuk, A. V., Syrbu, N. S., et al. (2019). Methane Anomalies, its Flux on the Sea-Atmosphere Interface and Their Relations to the Geological Structure of the South-Tatar Sedimentary Basin (Tatar Strait, the Sea of Japan). *Mar. Geophys Res.* 40, 581–600. doi:10.1007/s11001-019-09389-3

Shakirov, R. B., Valitov, M. G., Syrbu, N. S., Yatsuk, A. V., Obzhirov, A. I., Mishukov, V. F., et al. (2020). Methane Fluxes at the Water-Atmosphere Interface in the Southern Tatar Strait of the Sea of Japan: Distribution and Variation. *Russ. Geol. Geophys.* 61 (9), 994–1006. doi:10.15372/RGG2019184

Shevchenko, G. V., Vilyanskaya, E. A., and Chastikov, V. N. (2011). Seasonal Variability of Oceanological Conditions in the Northern Part of the Tatar Strait. *Russ. Meteorol. Hydrol.* 36 (1), 55–64. doi:10.3103/S1068373911010080

Smith, S. P., and Kennedy, B. M. (1983). The Solubility of Noble Gases in Water and in NaCl Brine. *Geochimica Cosmochimica Acta* 47 (3), 503–515. doi:10.1016/0016-7037(83)90273-9

Snyder, G. T., Sano, Y., Takahata, N., Matsumoto, R., Kakizaki, Y., and Tomaru, H. (2020). Magmatic Fluids Play a Role in the Development of Active Gas Chimneys and Massive Gas Hydrates in the Japan Sea. *Chem. Geol.* 535, 119462. doi:10.1016/j.chemgeo.2020.119462

Takahata, N., Agarwal, M., Nishizawa, M., Shirai, K., Inoue, Y., and Sano, Y. (2005). Helium-3 Plume over the East Pacific Rise at 25°S. *Geophys. Res. Lett.* 32 (11). doi:10.1029/2005GL023076

Takahata, N., Sano, Y., Horiguchi, K., Shirai, K., and Gamo, T. (2008). Helium Isotopes of Seawater in the Japan Sea. *J. Oceanogr.* 64 (2), 293–301. doi:10.1007/s10872-008-0023-3

Talley, L. D., Lobanov, V., Ponomarev, V., Salyuk, A., Tishchenko, P., Zhabin, I., et al. (2003). Deep Convection and Brine Rejection in the Japan Sea. *Geophys. Res. Lett.* 30 (4). doi:10.1029/2002GL016451

Tarasyuk, S. N. (2002). "Survival of Yellowfin Sole (*Limanda aspera* Pallas) in the Northern Part of the Tatar Strait (Sea of Japan) during the Second Half of the 20th Century," in *Paper Presented at PICES-GLOBEC International Program on Climate Change and Carrying Capacity*. Editors B. C. Sidney and H. P. Batchelder (Canada, PICES Scientific Report No.).

Velikanov, A. Y. (2016). Pacific Sardine (Sardinops Melanostictus) Migrations to the Shores of Sakhalin Island in the 20th-Early 21st Centuries. *J. Ichthyol.* 56 (5), 715–727. doi:10.1134/S0032945216040147

Vereshchagina, O. F., Korovitskaya, E. V., and Mishukova, G. I. (2013). Methane in Water Columns and Sediments of the North Western Sea of Japan. *Deep Sea Res. Part II Top. Stud. Oceanogr.* 86-87, 25–33. doi:10.1016/j.dsr2.2012.08.017

Wessel, P., Luis, J. F., Uieda, L., Scharroo, R., Wobbe, F., Smith, W. H. F., et al. (2019). The Generic Mapping Tools Version 6. *Geochem. Geophys. Geosyst.* 20 (11), 5556–5564. doi:10.1029/2019GC008515

Wiesenburg, D. A., and Guinasso, N. L. (1979). Equilibrium Solubilities of Methane, Carbon Monoxide, and Hydrogen in Water and Sea Water. *J. Chem. Eng. Data* 24 (4), 356–360. doi:10.1021/je60083a006

Yamamoto, S., Alcauskas, J. B., and Crozier, T. E. (1976). Solubility of Methane in Distilled Water and Seawater. *J. Chem. Eng. Data* 21 (1), 78–80. doi:10.1021/je60068a029

Yapa, P. D., Zheng, L., and Chen, F. (2001). A Model for Deepwater Oil/Gas Blowouts. *Mar. Pollut. Bull.* 43 (7–12), 234–241. doi:10.1016/S0025-326X(01)00086-8

Yatsuk, A., Shakirov, R., Gresov, A., and Obzhirov, A. (2020). Hydrocarbon Gases in Seafloor Sediments of the Tatar Strait, the Northern Sea of Japan. *Geo-Mar. Lett.* 40, 481–490. doi:10.1007/s00367-019-00628-5

Conflict of Interest: The authors declare that the research was conducted in the absence of any commercial or financial relationships that could be construed as a potential conflict of interest.

Publisher's Note: All claims expressed in this article are solely those of the authors and do not necessarily represent those of their affiliated organizations, or those of the publisher, the editors, and the reviewers. Any product that may be evaluated in this article, or claim that may be made by its manufacturer, is not guaranteed or endorsed by the publisher.